Rigorous theory of the radiative and gain characteristics of silicon and germanium lasing media

Hanqing Wen and Enrico Bellotti*

Department of Electrical and Computer Engineering, Boston University, 8 Saint Mary's Street, Boston, Massachusetts 02215, USA

(Received 16 September 2014; revised manuscript received 1 December 2014; published 14 January 2015)

A generalized numerical model for the phonon-assisted optical interband transition based on the Green's function formalism was developed and implemented to investigate optical processes in germanium and silicon media intended for on-chip light emitter and laser applications. High-fidelity full band structures obtained from the empirical pseudopotential method, self-energies, and the corresponding spectral density functions for the phonon-perturbed electron and holes have been computed numerically as a function of strain, temperature, and doping level. Validation has been carried out by showing the model's ability to accurately reproduce the measured temperature dependent absorption coefficient data for both germanium and silicon. Absorption coefficients, radiative recombination rates of germanium and silicon active media were investigated with different biaxial tensile strain, doping concentrations and injection conditions. Furthermore, when the model is employed to compute the optical gain in strained germanium, we find that the use of tensile strain and high injection are the preferable approaches to obtain population inversion. At the same time, strong absorption from the spin-orbit to the heavy-hole band limits the maximum injection density that can be applied. Finally, when applied to study silicon, the proposed model also successfully reproduces the experimentally observed radiative recombination peak due to the two-phonon process.

DOI: 10.1103/PhysRevB.91.035307 PACS number(s): 78.20.Bh, 78.60.Fi, 78.66.Db

I. INTRODUCTION

As a result of the ongoing activities to develop light emitter and laser structures compatible with standard silicon processes, a renewed effort has been devoted to study germanium (Ge) and silicon (Si) optical properties. Particular attention has been paid to understand how the optical properties of these materials change under the effect of strain and doping [1–4]. On the experimental side, attempts to develop Ge-based lasers have leveraged the fact that using the combination of tensile strain and high doping a significant enhancement of the direct radiative recombination rate could be obtained [5–7], and the optimum strain to fulfill the lasing conditions in Ge has also been studied theoretically [8]. More exotic approaches based on membranes are also being explored [9,10], which have demonstrated possible ways of achieving direct band gap in Ge. At the same time Si light emitters [11,12] based on avalanche processes have made the development of microdisplays possible [13]. The present work intends to contribute to this effort by achieving three main objectives. First, we intend to develop an appropriate formalism to study the optical absorption and radiative properties of strained Ge and Si that goes beyond the conventional second-order perturbation theory (SOPT). Although, SOPT has been employed to analyze the indirect processes for many years [14], it is difficult to properly handle the divergences when the energy of transitions is not known *a priori*. As a result, it may not be possible to apply this approach to all the possible cases consistently. The proposed model, however, is based on the Green's function formalism [15], in which we employ the spectral density functions to describe the broadening of the states involved in the transitions due to different physical processes, therefore avoiding the divergence difficulties in SOPT naturally [16]. Second, we intend to develop a numerical approach suitable to compute the aforementioned properties using the full band structure of the material. This approach eliminates the approximations introduced by the analytical models based on parabolic or nonparabolic bands, makes it possible to analyze the behavior of the material when a significant portion of carriers populate the states far above the band edge [11,14], and naturally includes the effects of valence-band warping and anisotropy, which is particularly important when evaluating the matrix elements of the radiative process. Finally, we apply the developed model to study strained Ge and Si, where it will be shown that the model can reproduce the experimental data for the temperature-depended absorption coefficient of relaxed material. Subsequently, strained materials will be further investigated in terms of energy- and temperature-dependent absorption coefficients and radiative recombination rates under different doping and injection conditions.

The manuscript is organized as follows. Section II will give a general description of the theoretical model including the Green's function formalism, the band structure calculation model, and the numerical implementations. Section III will discuss the results obtained for Ge and Si, and finally, Sec. IV will deliver the conclusion. Theoretical derivation of the absorption coefficient and radiative recombination rate formulas can be found in Appendix.

II. THEORETICAL MODEL AND IMPLEMENTATION

In this section, the theoretical model used in this work and its numerical implementations are presented. In particular, we first outline the main ideas behind the Green's function model for the phonon-assisted (PA) process, then the approach used to compute the electronic structure is described and finally the details of the numerical implementations are explained. The derivation of the formulas used in this section is stated in Appendix.

*bellotti@bu.edu

A. Theory

As was pointed out earlier, the main motivation of using the Green's function approach lies in trying to avoid the numerical and convergence issues arising from conventional SOPT [14]. However, a number of investigations that have employed the Green's function theory were mainly focused on computing the recombination rates of Auger processes mediated by the Coulomb interaction [16–18]. In the case of radiative recombination processes, dipole interactions, where the electromagnetic field interacts with electrons and holes, need to be taken into account instead. Specifically, in this work, PA indirect photon absorption and emission processes are studied. Although the derivation of suitable expressions to compute PA and impurity-assisted Auger recombination rates using quasiequilibrium Green's function formalism (Matsubara method) have already been presented by Takeshima [19], little or no information is available on the analogous formula for the PA radiative recombination/absorption processes, except for an expression reported in Ref. [17] [see Eq. (2.4)]. In the work of Kwong *et al.* [20], though the phonon-assisted process was studied along with the electron-hole plasma interaction using quasiequilibrium Green's function, only a phenomenological expression was employed to model the PA. On the other hand, Bardyszewski and Yevick [21] proposed an alternative way to describe the optical recombination in the context of electron-hole plasma interaction using nonequilibrium Green's functions (Keldysh method), which gives good agreement with the experimental data but requires the inclusion of dynamic screening in the model. This leads to a significant increase of computational complexity for the full band calculation while only a minor correction to the optical gain can be achieved. Since our main focus is on the PA processes and the full band structure effects, in the present work, we employed a Thomas-Fermi static screening and ignored the additional correction due to the electron-plasma interaction.

Here, we only recorded the final expressions of absorption coefficient and radiative recombination rate for the PA indirect transition based on the Matsubara method. For detailed information, salient points of the derivation are summarized in Appendix, which illustrates the foundation of the model, and sheds light on the important approximations made in the theory.

The absorption coefficient between band 1 and 2 for a photon energy of $\hbar\omega_{\rm ph}$ is

$$\begin{aligned}\alpha_{12}(\hbar\omega_{\rm ph}) = {} & \frac{2\pi}{n_r c_0 v \omega_{\rm ph}\epsilon_0}\sum_{\mathbf{k}}|P_{1,2}(\mathbf{k})|^2 \\ & \times\int dE_1'\int dE_2'(\Theta(E_1')-\Theta(E_2')) \\ & \times\delta(\mu_c-\mu_v+E_2'-E_1'-\hbar\omega_{\rm ph}) \\ & \times{\rm Im}G_{l_1}^R(\mathbf{k},E_1'){\rm Im}G_{l_2}^R(\mathbf{k},E_2'). \end{aligned} \quad (1)$$

The radiative recombination rate per unit volume per energy interval from band 2 to band 1 is then computed as [22]

$$\begin{aligned}R_{21}(\hbar\omega_{\rm ph}) = {} & \frac{2n_r\omega_{\rm ph}}{\pi\hbar c_0^3 v\epsilon_0}\sum_{\mathbf{k}}|P_{1,2}(\mathbf{k})|^2 \\ & \times\int dE_1'\int dE_2'\Theta(E_2')(1-\Theta(E_1')) \\ & \times\delta(\mu_c-\mu_v+E_2'-E_1'-\hbar\omega_{\rm ph}) \\ & \times{\rm Im}G_{l_1}^R(\mathbf{k},E_1'){\rm Im}G_{l_2}^R(\mathbf{k},E_2'), \end{aligned} \quad (2)$$

where $e, m_0, v, \omega_{\rm ph}, \epsilon, \hat{\mathbf{e}}$ are the electron charge, electron mass, volume of the crystal, frequency of the photon, dielectric function, and polarization of the photon, respectively. $P_{1,2}(\mathbf{k})$ is the matrix element for the dipole interaction defined in Eq. (A8), and $\Theta(E)$ is the Fermi factor defined as $\Theta(E) = 1/[1+e^{E/(k_BT)}]$, where the energy E is measured from the corresponding quasi-Fermi level. ${\rm Im}G_l^R$ is the spectral density function for band l.

B. Electron self-energy

In order to evaluate Eqs. (1) and (2), the specific form of electron Green's function G^R needs to be known. To this end, the electron Matsubara functions in Eqs. (A32) and (A33) are expanded by using Dyson's equation with a suitable electron-phonon interaction potential. As a consequence, one can get a closed form of Matsubara Green's functions $g_{2,3}$ and $g_{4,1}$ [see Eqs. (A32) and (A33)] when only the first-order term in the expansion is retained. Since the procedure is well established and can be found in most textbooks on Green's function theory (see Chap. 5 of Ref. [15] and Ref. [23]), we only present the results here. Specifically, we have

$$\begin{aligned}&{\rm Im}G_{l_i}^R(\mathbf{k},E) \\ &\quad = -\frac{1}{\pi}\frac{{\rm Im}\Sigma_i(\mathbf{k},E)}{[E-E_i(\mathbf{k})-{\rm Re}\Sigma_i(\mathbf{k},E)]^2+[{\rm Im}\Sigma_i(\mathbf{k},E)]^2} \end{aligned} \quad (3)$$

and

$$\begin{aligned}&{\rm Im}\Sigma_i(\mathbf{k},E) \\ &\quad = -\pi\sum_v\int\frac{d\mathbf{k}'}{(2\pi)^3}|g_v(\mathbf{k}'-\mathbf{k})|^2 B_{ii}(\mathbf{k},\mathbf{k}') \\ &\qquad \times\{[1+P(\hbar\omega_v)-\Theta(E-\hbar\omega_v)]\delta(E-\hbar\omega_v-E_i(\mathbf{k}')) \\ &\qquad +[P(\hbar\omega_v)+\Theta(E+\hbar\omega_v)]\delta(E+\hbar\omega_v-E_i(\mathbf{k}'))\}, \end{aligned} \quad (4)$$

where $B_{ii}(\mathbf{k},\mathbf{k}')$ is the overlap integral between the lattice periodic part of the Bloch states with wave vectors $\mathbf{k}$ and $\mathbf{k}'$. The matrix elements $g_v(\mathbf{k}'-\mathbf{k})$ for the acoustic, piezoelectric, nonpolar optical and polar optical carrier-phonon interaction, respectively, are given by [24]

$$|g_1(\mathbf{q})|^2 = \frac{\Xi_d^2\hbar\omega_{ac}(\mathbf{q})}{2c_l}\frac{q^4}{(q^2+\lambda^2)^2}, \quad (5)$$

$$|g_2(\mathbf{q})|^2 = \frac{e^2\hbar\omega_{ac}(\mathbf{q})}{2\epsilon}K_{\rm AV}^2\frac{q^2}{(q^2+\lambda^2)^2}, \quad (6)$$

$$|g_3(\mathbf{q})|^2 = \frac{\hbar D^2 v_s^2}{2\omega_{op}(\mathbf{q})\bar{c}}\frac{q^4}{(q^2+\lambda^2)^2}, \quad (7)$$

$$|g_4(\mathbf{q})|^2 = \frac{e^2\hbar\omega_{op}(\mathbf{q})}{2\epsilon^*}\frac{q^2}{(q^2+\lambda^2)^2}. \quad (8)$$

Here, c_l and c_t are the longitudinal and transverse elastic constants, respectively, $\bar{c}$ is the average elastic constant $\bar{c} = c_l/3+2c_t/3, v_s$ is the sound velocity, and ϵ^* is the effective inverse dielectric constant $\epsilon^{*-1} = \epsilon_\infty^{-1}-\epsilon_0^{-1}$. The phonon

TABLE I. Material parameters used in the calculation of electron self-energy for electron-phonon interaction. Values of the parameters are obtained or derived from Refs. [26,27].

Parameter	Unit	Ge	Si
v_l	10^5 cm/s	5.31	9.0
v_t	10^5 cm/s	3.61	5.41
c_l	10^{11} dyn/cm^2	12.85	16.58
c_t	10^{11} dyn/cm^2	6.68	7.96
ϵ_0	–	16.2	11.9
ϵ_∞	–	16.2	11.9
$\hbar\omega_{\rm op}$	meV	37.04	61.2
Ξ_d	eV	8.1	7.1
$K_{\rm AV}$	–	0	0
$D(L_{6,c})$	10^8 eV/cm	9.05	9.35
$D(\Gamma_v)$	10^8 eV/cm	12.17	13.24

occupation factor $P(\hbar\omega_v)$ is given by the Bose-Einstein distribution, which is $P(\hbar\omega_v) = 1/[e^{\hbar\omega_v/(k_BT)} - 1]$. The coupling constants of these interactions are defined as Ξ_d, the effective deformation potential; D is the optical coupling constant and $K_{\rm AV}$ is the average electromechanical coupling coefficient. In this work, since both Si and Ge are centrosymmetric crystals, the corresponding $K_{\rm AV} = 0$ [25]. For other material systems that do not posses this property, the piezoelectric scattering is nonzero and its contribution to the self-energy should be included. To simplify the calculation, we further assumed a linear dispersion for LA phonons and a constant phonon energy for optical phonons [23], which is a good approximation in silicon and germanium.

Values of these constants used in this work can be found in Table I. As it was stated above, the Thomas-Fermi screening has been adopted in modeling the electron-electron interaction for its simplicity. Unlike in the Auger process, where the electron-electron interaction is at the center of interest thus requiring the use of a more rigorous screening model, in the case of absorption and radiative recombination, this interaction is usually of less importance, therefore the Thomas-Fermi model is generally considered as a good approximation [23].

C. Band Structures

Since the full band structures are crucial in order to include the band nonparabolicity effect in the calculation, a reliable model of band structures is highly desirable. In the literature, electronic structure calculations for both Si and Ge have been carried out either within the density-functional-theory (DFT) framework or using the empirical pseudopotential method (EPM), whereas in the former calculation scheme, all-electron approaches and the state-of-the-art GW approaches [28] have produced many high-quality band structures. On the other hand, the EPM scheme, though less accurate than the *ab initio* techniques, is also widely used in the community due to its simplicity, high computational efficiency and the flexibility that the resulting electronic structures can be optimized to closely match the experimental and/or the *ab initio* results. Furthermore, the number of plane waves used to expand the electron wave functions in EPM is finite, which greatly simplifies all the calculations involving the overlap integral. As a result, in this work, we intend to compute the band structures from EPM. The key information needed in the EPM model is the screened effective atomic potential for each atomic species in the material. The determination of these atomic potentials in standard approaches has relied on the fitting of form factors in order to reproduce a small set of band features that can be known experimentally. Unlike the case of compound materials, for elemental semiconductors, such as Si or Ge, the form factors correspond to the matrix elements of the potential operators. Although, the form factors only need to be known on a discrete number of wave vectors, the knowledge of the functional dependence [29] of the screened atomic potential on the wave vector is actually paramount to obtain an electronic structure that can accurately reflect the effect of strain [30] and carrier-phonon interaction [31]. In this work, we have determined the screened atomic potentials for both Si and Ge so that the calculated electronic structures reproduce not only the correct energy transitions, but also the effective masses of electrons and holes and the hydrostatic deformation potentials. Besides the screened atomic potentials, a spin-orbit correction is also considered in our EPM model since the effect is significant in Si as well as in Ge. The crystal Hamiltonian is therefore given by

$$H = \left[\frac{\hbar^2}{2m_0}\nabla^2 + V_{\rm LOC}(\mathbf{r})\right] + H_{\rm SO} \tag{9}$$

in which the second term in Eq. (9) is the spin-orbit part of the Hamiltonian. The relativistic correction for a state with wave vector $\mathbf{k}$ is introduced as a perturbation term, and the spin-orbit matrix elements are given by [32–34]

$$\begin{aligned}\langle \mathbf{K}_{i,v}|\boldsymbol{H}_{\mathbf{SO}}|\mathbf{K}_{j,v'}\rangle &= \boldsymbol{\sigma}_{vv'}\cdot(\mathbf{K}_i\times\mathbf{K}_j)\\ &\quad\times[\lambda^A\sin(\mathbf{G}_i-\mathbf{G}_j)\cdot\tau - i\lambda^S\sin(\mathbf{G}_i-\mathbf{G}_j)\cdot\tau],\end{aligned} \tag{10}$$

where $\boldsymbol{\sigma}_{vv'}$ is the Pauli matrix, $\mathbf{G}_i$ and $\mathbf{G}_j$ are the reciprocal lattice vectors, $\mathbf{K}_{i,j} = \mathbf{G}_{i,j} + \mathbf{k}$, and τ is the atomic position vector. The symmetric and antisymmetric spin parameters λ^S and λ^A are given by

$$\lambda^S = \frac{(\lambda_1+\lambda_2)}{2}, \tag{11}$$

$$\lambda^A = \frac{(\lambda_1-\lambda_2)}{2}, \tag{12}$$

where λ_1,λ_2 are defined as

$$\lambda_1 = \mu\boldsymbol{B}^{(1)}_{nl}(K_i)\boldsymbol{B}^{(1)}_{nl}(K_j), \tag{13}$$

$$\lambda_2 = \gamma\mu\boldsymbol{B}^{(2)}_{nl}(K_i)\boldsymbol{B}^{(2)}_{nl}(K_j). \tag{14}$$

The parameter γ is set to be the ratio of the spin-orbit energy of the free cation and anion atoms [35] ($\gamma = 1$ for Si and Ge), and μ has to be adjusted to obtain the correct spin-orbit energy for the material. The values of $\boldsymbol{B}^{(i)}_{nl}(k)$ are then computed for all the atomic species i in the crystal according to

$$\boldsymbol{B}^{(i)}_{nl}(k) = C\int_0^\infty \boldsymbol{j}_l(kr)\boldsymbol{R}^{(i)}_{nl}(r)r^2dr, \tag{15}$$

where $\boldsymbol{j}_l(kr)$ is the spherical Bessel function of order l, $\boldsymbol{R}^{(l)}_{nl}(r)$ is the atomic wave function corresponding to the quantum

TABLE II. Optimized parameters of the local potential model.

Parameter	Unit	Ge	Si
V_0	Ry	−0.5303	−0.7000
V_3	Ry	−0.2425	−0.2177
V_8	Ry	0.0210	0.064 84
$V_1 1$	Ry	0.0479	0.079 82
$V_1 9$	Ry	0.0	0.0
γ	–	1.0	1.0
μ	–	0.00142	0.0115

numbers n and l, and C is a constant [34] that satisfies

$$\lim_{k\to 0} \frac{\boldsymbol{B}_{nl}^{(i)}(k)}{k} = 1. \tag{16}$$

We note that in Eq. (15), the formulation used for $\boldsymbol{R}_{nl}^{(l)}(r)$ is crucial to facilitate the evaluation of $\boldsymbol{B}_{nl}^{(i)}(k)$. In the present work, $\boldsymbol{R}_{nl}^{(l)}(r)$ is expanded through a set of suitable basis functions obtained with the Roothaan-Hartree-Fock method [36], and consequently, $\boldsymbol{B}_{nl}^{(i)}(k)$ can be calculated according to an analytical expression [37].

The parameters of the local potentials and the spin-orbit corrections employed in the calculation of Si and Ge band structures are reported in Table II. The functional dependence of the screened atomic potentials on the wave vector is numerically described by a spline interpolation, which is presented in Fig. 1 for a specific case. Notice that the features of the interpolation depend on the behavior of the electronic structure under strain. When calculating the band structures, the Hamiltonian in Eq. (9) is diagonalized using a closed set of 226 spinors (113 plane waves) for a suitable set of $\boldsymbol{k}$ vectors. As it will be explained in the next section, this set of $\boldsymbol{k}$ vectors is optimized for each band in order to capture the details of the band edges while maintaining the data sets of wave-function expansion coefficients in a manageable size. The calculated band structures of relaxed Ge and Si using

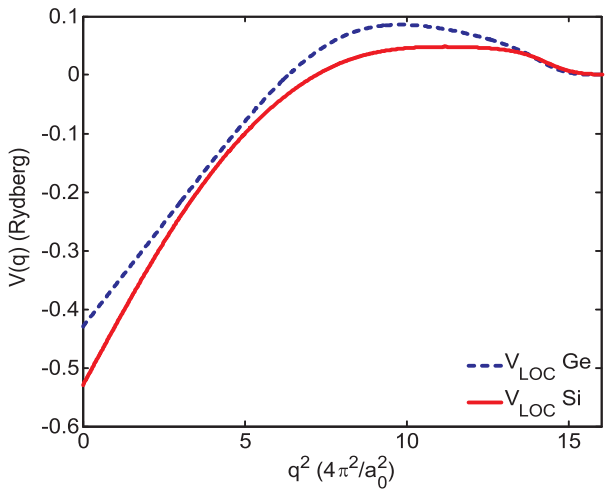

FIG. 1. (Color online) Wave-vector-dependent screened atomic potential employed in the calculation of Si and Ge electronic structure. a_0 is the lattice constant.

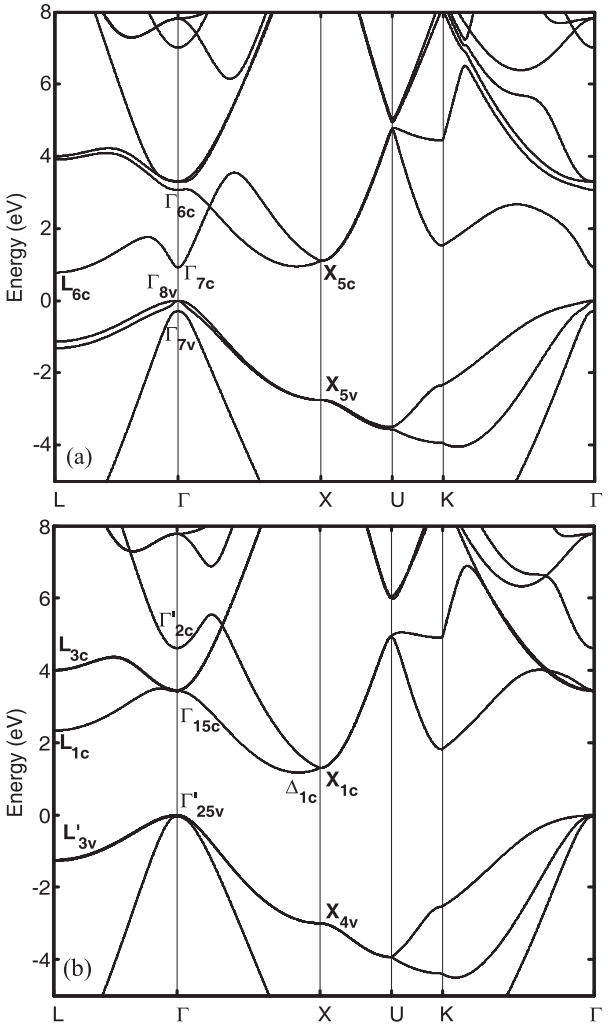

FIG. 2. Calculated electronic structures of relaxed (a) Ge and (b) Si.

the EPM approach outlined above, are presented in Fig. 2. For further comparison, the fundamental gaps and effective masses in different valleys are listed in Tables III and IV for Ge and Si, respectively, from GW calculations, experimental data, and this work. To conclude this section, in Fig. 3, we calculated the change of the fundamental energy gaps as a function of the applied strain. A strain applied along the [100] direction is considered as the case of the growth of Ge on [100] Si. Figure 3(a) presents the calculated valence and conduction band energies of Ge at the Γ, Δ_{100}, Δ_{001}, and $L_{6,c}$ points in the first Brillouin zone. We notice that for relaxed Ge, the calculated energy separation between $\Gamma_{7,c}$ and $L_{6,c}$ is approximately 0.143 meV, while this number between the minima at Δ_{100} and $L_{6,c}$ is about 0.174 meV. Consequently, the intervalley energy difference between Δ_{100} and $\Gamma_{7,c}$ is only around 30 meV, which gives rise to the possibility of changing Ge into a direct gap material. Indeed, as is shown in Fig. 3(a), when applying a tensile strain along [100] direction, the energy of the $\Gamma_{7,c}$ valley drops more rapidly than that of the $L_{6,c}$ valley, and at the tensile strain of 2% the two valleys have the same energy, effectively transiting the material into a direct band-gap material. Figure 3(b) gives the results of the

TABLE III. Calculated and experimental energy gaps and effective masses for Ge.

Parameter	Unit	This Work	GW + SO[a]	Exp.[b]
Γ_{6v}	eV	−12.2	−12.53	−12.66
Γ_{7v}	eV	−0.291	−0.32	−0.3
Γ_{7c}	eV	0.92	0.38	0.9
Γ_{6c}	eV	3.3	2.89	3.25
X_{5c}	eV	1.1	1.16	1.16
L_{6c}	eV	0.78	0.54	0.76
L_{3c}	eV	3.9	4.18	4.2
$m_e^{L\perp}$	m_0	0.09		0.082
$m_e^{L\parallel}$	m_0	1.45		1.57
m_e^{Γ}	m_0	0.047		0.038
m_{hh}^{Γ} [100]	m_0	0.286		0.284
m_{lh}^{Γ} [100]	m_0	0.061		0.0438
m_{so}^{Γ} [100]	m_0	0.132		0.095
m_{hh}^{Γ} [110]	m_0	0.544		0.376
m_{lh}^{Γ} [110]	m_0	0.054		0.0426
m_{so}^{Γ} [110]	m_0	0.132		0.095
m_{hh}^{Γ} [111]	m_0	0.736		0.352
m_{lh}^{Γ} [111]	m_0	0.054		0.043
m_{so}^{Γ} [111]	m_0	0.132		0.095

[a]Values calculated using GW + SO from Ref. [28].
[b]Experimental values from Ref [27]. m_0 is the electron mass.

same calculation for Si and one can notice that the minimum energy of the four Δ valleys lying in plane (100) is higher than the two Δ valleys along the [100] direction where a tensile strain is applied. It is also obvious that regardless of the strain magnitude, the $L_{6,c}$ point is always above the Δ valleys and the energy of the Γ point (not shown) never falls below 3 eV.

TABLE IV. Calculated and experimental energy gaps and effective masses for Si.

Parameter	Unit	This Work	GW + SO[a]	Exp.[b]
Γ_{1v}	eV	−12.41	−11.63	−12.5
Γ'_{25v}	eV	−0.042	−0.05	−0.044
Γ_{15c}	eV	3.36	3.28	3.34
Δ_{1c}	eV	1.17		1.17
X_{1c}	eV	1.29	1.43	1.3
L_{1c}	eV	2.23	2.13	2.04
L_{3c}	eV	4.0	4.16	3.9
$m_e^{\Delta\perp}$	m_0	0.2		0.19
$m_e^{\Delta\parallel}$	m_0	0.928		0.92
m_e^{Γ}	m_0	0.4		
m_{hh}^{Γ} [100]	m_0	0.27		0.537
m_{lh}^{Γ} [100]	m_0	0.22		0.153
m_{so}^{Γ} [100]	m_0	0.24		0.234
m_{hh}^{Γ} [110]	m_0	0.56		0.537
m_{lh}^{Γ} [110]	m_0	0.15		0.153
m_{so}^{Γ} [110]	m_0	0.24		0.234
m_{hh}^{Γ} [111]	m_0	0.69		0.537
m_{lh}^{Γ} [111]	m_0	0.14		0.153
m_{so}^{Γ} [111]	m_0	0.24		0.234

[a]Values calculated using GW + SO from Ref. [28].
[b]Experimental values from Ref [27]. m_0 is the electron mass.

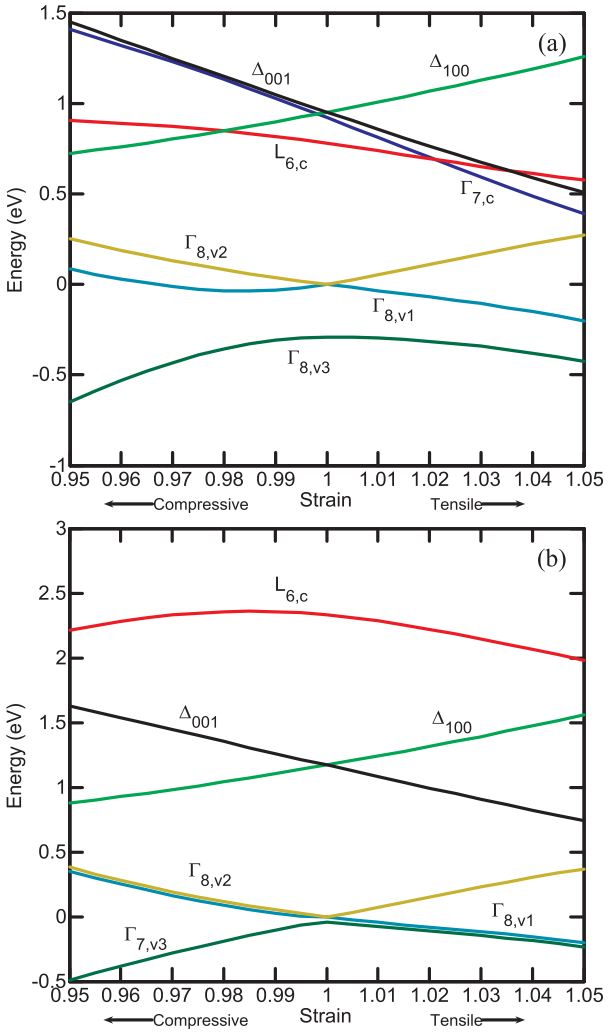

FIG. 3. (Color online) Calculated fundamental energy gaps of (a) Ge and (b) Si under compressive and tensile biaxial strain.

D. Numerical implementation

One difficulty in numerically evaluating the Green's function is related to the integration of the delta function in Eq. (4) or equivalently, the computation of a two-dimensional integral on a constant-energy surface in momentum space. In our case, since the full band structures are employed, the lack of an analytical expression for the energy dispersion $E(\mathbf{k})$ makes this integration even more challenging. In this work, we adopted the tetrahedron method where the electron energy $E(\mathbf{k})$ and other $\mathbf{k}$-dependent quantities are linearly interpolated throughout each tetrahedron using the corresponding values at the four vertices. This approach has proven to be efficient and accurate [38,39]. Although higher order interpolation schemes, such as quadratic interpolation, can provide even more accurate results [40], their complex implementation and computational load make the linear interpolation method more appealing. To reduce the error introduced by the numerical implementation, while maintaining a reasonable computation time, instead of using a uniform mesh, we employed a band-adaptive nonuniform mesh [39] by considering the specific features of each band involved in a transition, where a

dedicated tetrahedron mesh is produced to optimize the energy interpolation. In this work, a tetrahedron mesh with 22 887 elements in the irreducible wedge (IW) is used to perform the integration of Eqs. (1) and (2), and another mesh with 8422 tetrahedrons is employed in the evaluation of Eq. (4) due to the different types of integrands in these equations. The convergence of the integration has been checked using meshes of different sizes. For example, a mesh of 32 560 tetrahedrons in IW provides essentially the same result as the mesh of 22 887 tetrahedrons with a maximum difference always below 5%. Finally, we want to point out that the realistic density of states involving four valence bands and eight conduction bands are evaluated on a 35 299 tetrahedron mesh for each strain configuration and lattice temperature. This information is later used in the calculation of quasi-Fermi energy under different doping/injection conditions.

As was mentioned in Appendix, when computing Eqs. (1) and (2), we have ignored the contribution of PA inter-band transition to the self-energy. As a result, the spectral density functions for the two bands $\mathrm{Im}G_{l_i}^R(\mathbf{k},E), i = 1,2$ are independent. Therefore, by using the two spectral density functions in Eqs. (1) and (2), one can actually analyze two-phonon events, where an electron is first scattered in the lower (upper) band, absorbs (emits) a photon and is eventually scattered by another phonon reaching its final state in upper (lower) band. Alternatively, if only one of the electron spectral density functions is used in Eqs. (3) and (4), leaving the other to be a delta function, one phonon event is considered instead. Consequently, if one considers all possible cases, direct, one-phonon and two-phonon PA events can be investigated. As will be shown in Sec. III B, the case of two-phonon processes is evaluated for Si, which is not possible with the traditional SOPT method.

As a final note, we want to point out that the matrix element that describes the dipole interaction in Eq. (A8) is a quantity averaged over all polarizations $\hat{\mathbf{e}}$. When the polarization effect needs to be studied, we will explicitly evaluate the matrix elements for a specific polarization state.

III. RESULTS AND DISCUSSION

In this section, we will discuss the results obtained by applying the method outlined in Sec. II to the calculation of the absorption coefficients and radiative recombination rates in relaxed and strained Ge and Si. A schematic of the important absorption paths in relaxed Ge is illustrated in Fig. 4.

A. Germanium

We first consider the case of relaxed and strained bulk Ge. Figure 5(a) presents the calculated photon-energy-resolved absorption coefficient in two sets of lines. The first set, on the right side of the plot, is for relaxed bulk Ge, and the second set, on the left side, is for 1.4% tensile strained bulk Ge. The solid lines (red color) represent the calculated absorption coefficient at the temperature of 77 K, while the dashed lines (green color), dash-dot lines (black color), and dash-two-dot lines (purple color) are for the temperatures of 150, 225, and 300 K, respectively. To validate the accuracy of our numerical model, the experimental data of the absorption

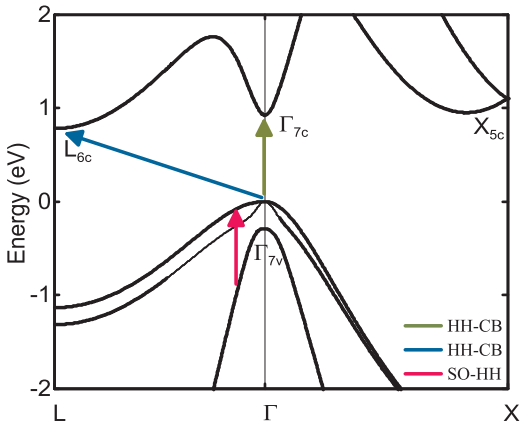

FIG. 4. (Color online) Detail of the calculated Ge electronic structure near the band edges including the direct, indirect HH-CB, and SO-HH transition paths for electrons. The absorption transition paths are represented by the arrows in the figure while the gain transitions are the reverse processes.

coefficient measured at 77 and 300 K [41] are included as well, which are represented by the open symbols (squares for 77 K and circles for 300 K). As one can see in Fig. 5(a), in the case of unstrained intrinsic Ge, the numerical results match very well with the experimental data for both 77 and 300 K in the whole range of the measured photon spectrum. These comparisons provide a high degree of confidence in the predictive ability of the numerical method and the reliability of our ensuing analysis of the strain effect on the absorption coefficients and radiative recombination rates. As an additional note, we would like to point out that for the results presented in this section, contributions of the transitions from LH and HH to the first conduction band are summed together because of the difficulties of separating one transition from the other in the presence of the band mixing between LH and HH under strain. Furthermore, since the higher conduction bands and lower valence bands are generally less populated, they provide a negligible correction to our results in the range of photon energy considered here. Consequently, they are selectively included in the calculation of optical transitions based on their relative carrier populations.

Comparing the absorption spectra for different lattice temperatures T in Fig. 5(a), it is apparent that when T decreases, at the same amount of tensile strain, the shape of the curves barely changes despite the fact that the curves tend to shift toward higher photon energy and the tail near the absorption edge shrinks. The shift of curves with temperature is consistent with the experimental data [27], where the increase of lattice temperature makes both direct and indirect band gaps shrink nearly uniformly. Additional information about the tails of the absorption curves can be obtained from Fig. 5(b), in which the contributions to the total absorption coefficient (solid lines) from the PA indirect (dashed lines) and direct (dash-dot lines) processes are plotted in two tensile strain configurations: $\epsilon = 0$ and 2.1% at 300 K for n-type Ge ($N_d = 10^{19}$ cm^{-3}). As is shown, the PA indirect transition from Γ_v to L_c states predominantly gives rise to the tails of absorption curves since the corresponding photon energy is just slightly above the indirect bang gap. When the absorbed

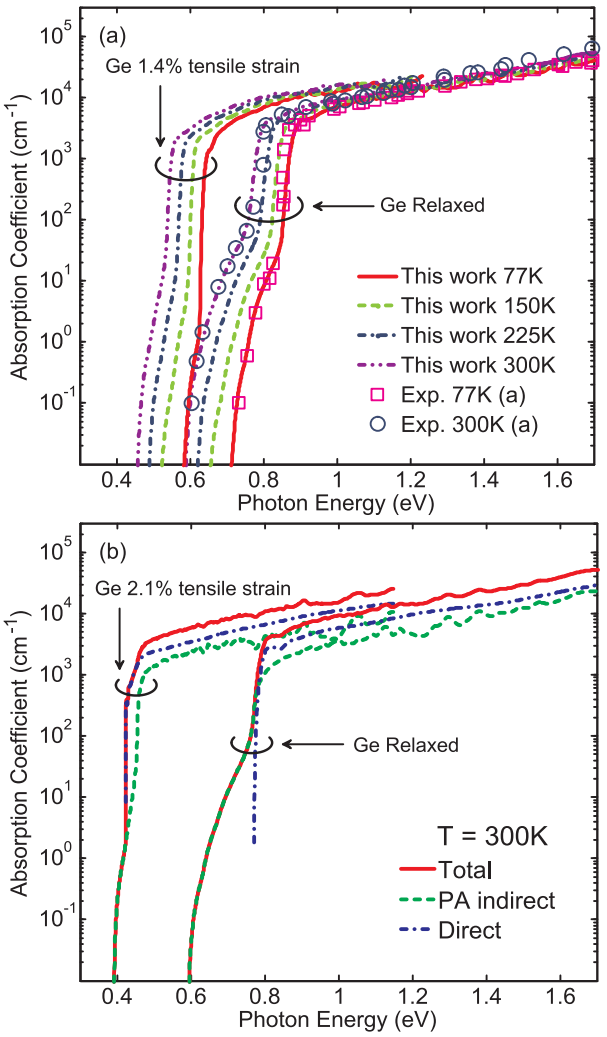

FIG. 5. (Color online) Absorption coefficient spectra of Ge calculated with the Green's function theory under different strains, doping, and lattice temperatures at thermal equilibrium. (a) Intrinsic Ge with relaxed lattice structure (right group) and with $\epsilon = 1.4\%$ biaxial tensile strained structure (left group) are compared with the measured data for intrinsic relaxed Ge at 77 K (open circles) and 300 K (open squares) [41]. The style and color of lines represent the corresponding lattice temperatures. (b) Results of $10^{19}\,\mathrm{cm}^{-3}$ n-doped Ge at 300 K with a tensile strain $\epsilon = 0$ (right group) and $\epsilon = 2.1\%$ (left group). The contributions from direct (dash-dot lines) and PA indirect processes (dashed lines) are compared with the total absorption coefficient (solid lines).

photon energy gets larger, the direct transition process starts to be dominant, resulting in a sudden increase in the absorption curves. Back to Fig. 5(a), due to the fact that at low temperature, the average number of phonons in the crystal decreases, the strength of indirect transitions is reduced as well. In both cases of relaxed ($\epsilon = 0\%$) and tensile strained material ($\epsilon = 1.4\%$), the indirect part in the total absorption gradually diminishes when T decreases from 300 to 77 K. In fact, for a tensile strain of $\epsilon = 1.4\%$ and a photon energy equal to the direct band gap, the indirect absorption process only accounts for about 2% of the total absorption at 77 K, whereas the number for the same process is 48% at 300 K. For the unstrained material ($\epsilon = 0$), although the indirect transition is weaker at lower temperature, the difference is not significant due to the relatively large energy separation between L_c and Γ_c valleys making the indirect transition consistently dominant.

From the analysis of the relaxed Ge band structure in Fig. 2(a), the phonon-assisted indirect transition generally can be divided into three contributions. The first one is from the Γ_v to L_c, which is largely responsible for the absorption at lower photon energy. A second contribution, coming from the Γ_v to X_c transition, which is only relevant when the photon energy is larger than the direct band gap. Finally, the last one, from the region around Γ_v to Γ_c, which is usually negligible due to the small matrix element for phonon scattering [see Eqs. (5)–(8)]. Although the PA transitions from Γ_v to L_c in relaxed Ge is the dominant absorption mechanism for the photons with energy between the fundamental indirect gap and the direct gap, it should be noted, however, that all the possible transitions need to be considered when the absorbed photon energy gets larger than the direct band gap. In fact, as demonstrated by the right group of lines in Fig. 5(b), for photon energies higher than the direct gap, even though the direct process is dominant, the indirect process still accounts for $\approx$41% of the total absorption making the PA process never negligible. This is in stark contrast to direct-gap materials, such as HgCdTe or InAsSb [42].

When a tensile strain is added to the system, as in the case of $\epsilon = 2.1\%$ in Fig. 5(b), the situation changes. It can be noticed that the tail of absorption spectrum, which is obvious in the curve obtained for relaxed Ge, fades as the strain increases. Indeed, as is shown in Fig. 3, when the tensile strain increases, the direct band gap shrinks faster than the indirect band gap, making the direct process gradually more important than its indirect counterpart and eventually becoming the dominant one. Specifically, at $\epsilon = 2.1\%$, the energy difference between the L_c and Γ_c valleys almost vanishes and the indirect tail of the absorption spectra completely merges into the direct part. This band-gap reduction also explains the shift of absorption edge to a lower photon energy under increasing tensile strain. The same trend can also be observed in Fig. 5(a) for the strain of $\epsilon = 0\%$ and 1.4%, where the tail significantly diminished in the latter case at all the lattice temperatures considered.

Besides the considerable effects of strain on the absorption behavior of Ge, it is also important to investigate its effect on the spontaneous radiative recombination rate spectra $R(\hbar\omega)$, which could provide additional insight in understanding the electroluminescence properties in both relaxed and strained materials. Figure 6(a) presents the computed spontaneous recombination rate $R(\hbar\omega)$ for bulk Ge under different strain conditions. The calculation is carried out under two kinds of n-type doping, $N_d = 10^{19}$ (solid lines) and $10^{20}\,\mathrm{cm}^{-3}$ (dashed lines) at a constant injection level of $\delta n = 10^{18}\,\mathrm{cm}^{-3}$. In Fig. 6(b), the same quantity is calculated under a constant n-type doping $N_d = 5 \times 10^{19}\,\mathrm{cm}^{-3}$ with two different injection levels $\delta n = 10^{18}$ (dashed lines) and $\delta n = 10^{19}\,\mathrm{cm}^{-3}$ (solid lines).

We first consider the case of constant injection presented in Fig. 6(a), where, because of the faster reduction of direct band gap than the indirect one under increasing tensile strain, the shoulder in the curve due to PA indirect processes shrinks and eventually merges into the peak corresponding to the

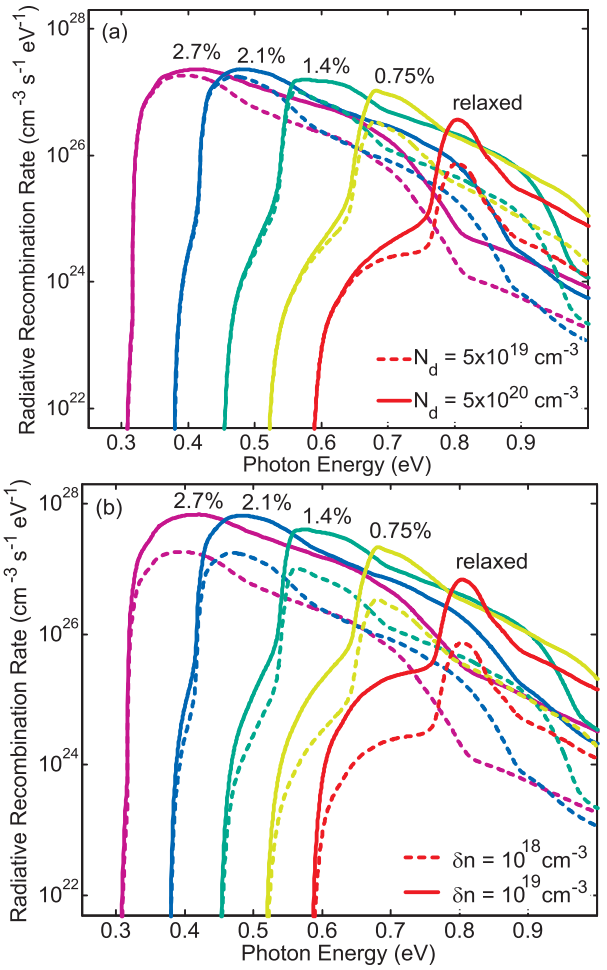

FIG. 6. (Color online) Radiative recombination rates of Ge at 300 K are computed under (a) different doping concentrations of 5×10^{19} (dashed lines) and 10^{20} cm^{-3} (solid lines) with the same injection of 10^{18} cm^{-3}; (b) different injection of 10^{18} (dashed lines) and 10^{19} cm^{-3} (solid lines) with the same n-doping of 5×10^{19} cm^{-3}. Numbers adjacent to each curve represent values of the corresponding biaxial tensile strain.

direct recombination process. This is clearly consistent with the previous results obtained for the absorption coefficients. Furthermore, identical reasoning also explains the enhancement effect of increasing doping concentration on the indirect radiative rate among different strain conditions. In fact, for relaxed Ge, due to the higher density of states and lower electron energy in L_c valley compared to Γ_c, a large fraction of electrons ionizing from the dopant will reside in L_c, making the enhancement of the PA indirect rate most significant in this case as is shown in Fig. 6(a). When the strain increases, more electrons tend to be in Γ_c valley, effectively lowering the enhancement of PA indirect process. Specifically, when increasing the doping concentration at $\epsilon = 2.1\%$, no visible change of the indirect radiative rate can be observed. Different behavior of increasing doping and injection concentrations can be investigated by comparing the results from Fig. 6(a) to that from Fig. 6(b), in which we can observe that by increasing the injection level, the PA process gets uniformly enhanced, while adding dopants hardly changes the radiative rate at the indirect absorption edge. This can be understood by considering the carrier distribution in the material. Similar to the aforementioned analysis, when extra donors are added to the system, as is the case of Fig. 6(a), more electrons will reside in L_c valley with the available hole concentration remaining the same in Γ_v. Consequently, only a small part of the additional electrons can recombine with holes due to the lack of additional holes in Γ_v. As a result, processes occurring at the indirect absorption edge are not significantly enhanced. When the carrier injection is increased instead, both electrons and holes are added to the system ensuring that the holes will not limit the recombination process. Therefore the PA indirect processes are enhanced in the whole spectrum, which gives rise to the differences between Figs. 6(a) and 6(b). For this reason, we can conclude that increasing the carrier injection level is a more efficient way to enhance the radiative recombination rate than using high doping. One should be aware that, however, at high injection, other recombination mechanisms, such as Auger recombination and free carrier absorption will become significant, which will in turn limit the radiative rate that could be achieved otherwise. It is also noteworthy that in both Figs. 6(a) and 6(b), when the tensile strain exceeds 2.1%, for which Ge becomes a direct band-gap material, there is no further increase of $R(\hbar\omega)$ due to strain.

To conclude the discussion about Fig. 6, we compare our results with the calculations performed by Virgilio and coworkers [2]. We noticed that our results are generally in agreement with those presented in Figs. 3 and 4 of Ref. [2], in which the radiative recombination rate was obtained using the SOPT. While the peak values and the trend of the recombination rate as a function of the photon energy from the two works are similar, a number of differences need to be mentioned. In particular, one can notice that sharp corners are present in the curves shown in Figs. 3 and 4 of Ref. [2]. We speculate that this may be due to the difference between the numerical approaches used in the calculations, especially the band structures for Ge. In fact, in our model, instead of considering the two principal transitions Γ_v to Γ_c and Γ_v to L_c separately, where a simple parabolic band approximation can be employed, we use the full band structure with all the possible recombination paths beyond the two major transitions covered. This methodological difference distinguishes our results from those in Ref. [2] by having a smooth interim region between the two peaks, where processes involving higher energy states in Γ_c, L_c, and X_c valleys are included.

The temperature dependencies of the radiative recombination rate for both relaxed and strained bulk Ge are examined in Fig. 7 with a 5×10^{19} cm^{-3} n-type doping and 10^{18} cm^{-3} carrier injection. Figure 7(a) presents the results for relaxed Ge and Fig. 7(b) provides the same information for a tensile strain of $\epsilon = 1.4\%$. As is shown in Fig. 7(a), two features representing the PA indirect and direct processes are presented for all four lattice temperatures. As the temperature decreases, the peak corresponding to the direct process is significantly reduced, while the shoulder that accounts for the indirect process practically retains its magnitude. Given that all of the four curves are computed using the same carrier concentration and assuming that the dopants are fully activated at all temperatures of interest, the change in the shape of the radiative rate can be understood by considering the relative carrier

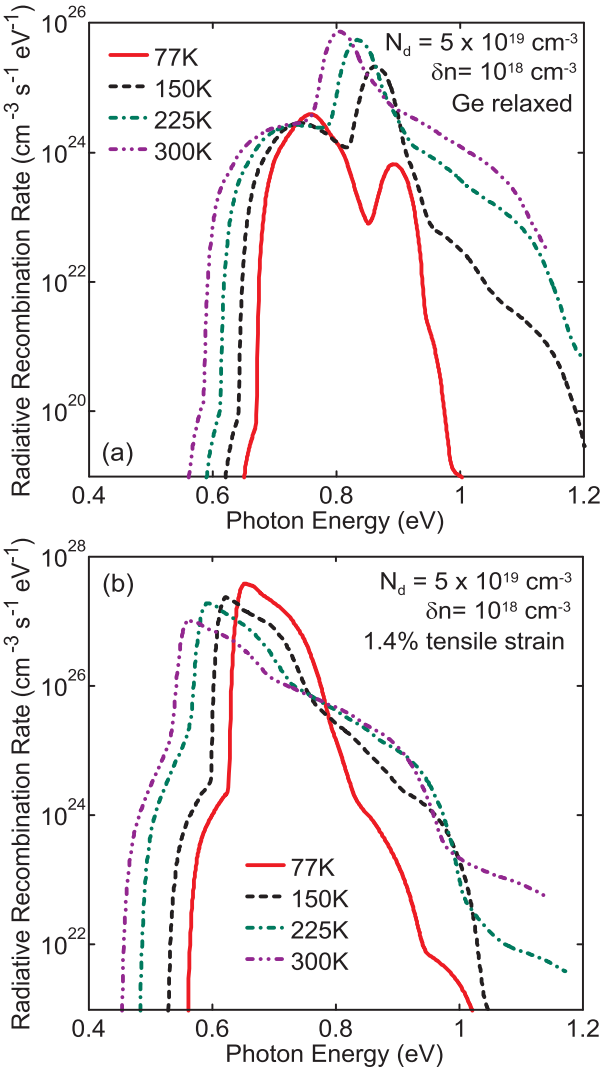

FIG. 7. (Color online) Temperature dependence of the radiative recombination rate in Ge obtained with biaxial tensile strain of (a) 0.0% and (b) 1.4% under the same doping/injection condition, i.e., 5×10^{19} cm^{-3}/10^{18} cm^{-3}.

distributions between the regions around Γ_c and L_c valleys. When the temperature decreases, the probability of occupation for electrons at higher energies in the conduction bands, particularly around the Γ_c valley, will be reduced significantly according to the quasi-Fermi distribution. This leads to a decrease of the direct radiative recombination rate, which drops from a peak value of 7.4×10^{25} cm^{-3} s^{-1} eV^{-1} at 300 K down to 6.5×10^{23} cm^{-3} s^{-1} eV^{-1} at 77 K. As to the indirect process, due to the large density of states and low electron energy in the L_c valley, the change in the electron occupation probability will not significantly impact the overall electron population in L_c valley, making the indirect recombination rate remain the same.

As it can be expected, the outcome of the same analysis changes if strain is added to the system. Figure 7(b) presents the calculated radiative recombination rate for $\epsilon = 1.4\%$ tensile strained Ge. We can notice that in this situation the peak corresponding to the direct process, in contrast with the case

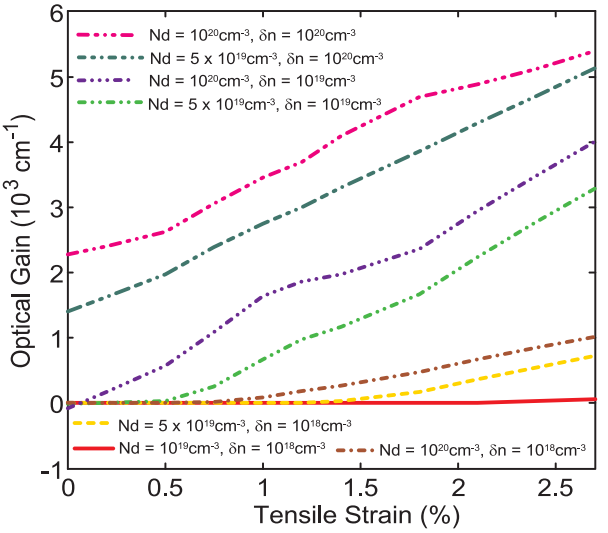

FIG. 8. (Color online) Peak values of optical gain coefficient in Ge as a function of strain conditions are calculated under various (doping,injection) levels (see legend). The gain is obtained solely from the transition between CB-HH and CB-LH with no free carrier absorption or spin-orbit to HH absorption included.

of relaxed Ge, increases in magnitude as the temperature decreases. This behavior can be traced back to the interplay between the L_c-Γ_c intervalley energy separation and the position of the electron quasi-Fermi energy. For relaxed Ge, due to the large energy separation between L_c and Γ_c, which is 0.143 eV compared to 0.047 eV for the case of $\epsilon = 1.4\%$, and the higher density of states of L_c valley, the electron quasi-Fermi level at 77 K is 0.07 eV below the direct band edge (at Γ_c), while in strained Ge, the electron quasi-Fermi level is 0.03 eV above the direct band edge. This leads to a Γ_c valley that is mostly empty at low temperatures in the former case, and an always partially filled Γ_c valley even at 77 K in the latter case. Additionally, for strained Ge when the temperature is reduced, in order to maintain the same carrier injection, more electrons will be concentrated around the Γ_c valley, making the radiative recombination happen in a very small range of photon energies. Consequently, the peak value of the recombination spectrum increases while the width of the peak shrinks. As to the relaxed structure, the lack of electrons in the Γ_c valley at low temperature makes the peak of the direct recombination fall dramatically. We noted that this carrier concentration effect also happened in indirect recombination from L_c, as observed in Fig. 7(a), but is much weaker.

One of the most compelling reasons to study the tensile strained Ge is the possibility to turn the indirect band-gap material into a direct one, potentially leading to the design of an efficient and CMOS-compatible laser. Therefore, in addition to the absorption coefficient, we have also calculated the optical gain of strained Ge at 300 K under various doping/injection conditions. Figure 8 shows the peak gain values as a function of applied tensile strain, where each curve represents a different doping/injection condition. It can be observed that the peak of the optical gain for a given doping/injection concentration increases almost linearly with the tensile strain, and a maximum value of 5400 cm^{-1} is

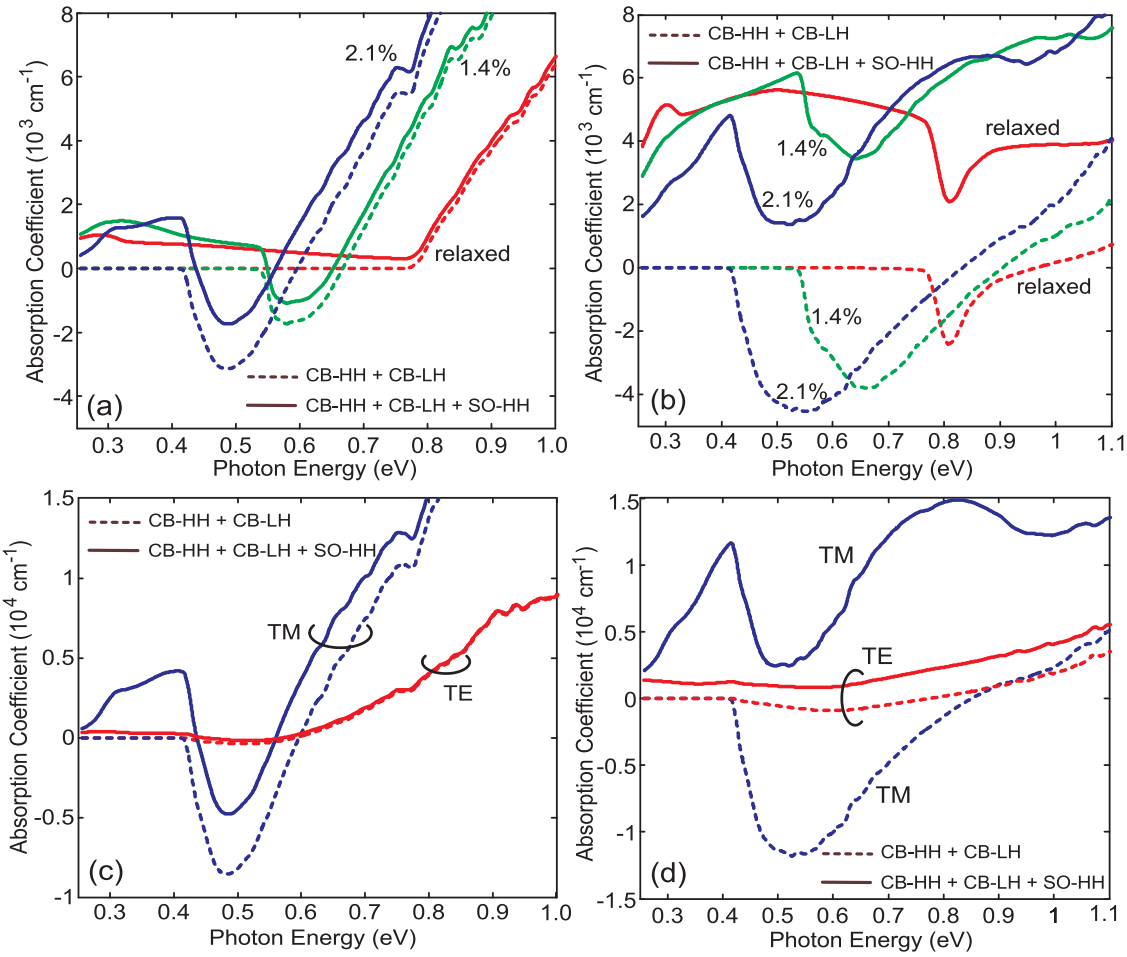

FIG. 9. (Color online) Absorption coefficient spectra for unpolarized [(a) and (b)] and polarized [(c) and (d)] light are examined with (doping, injection) of (10^{20} cm^{-3},10^{19} cm^{-3}) [for (a) and (c)] and (10^{20} cm^{-3},10^{20} cm^{-3}) [for (b) and (d)]. Throughout (a)–(d), dashed lines represent the results from CB-HH and CB-LH transitions, and the solid lines give the total absorption by adding the results from SO-HH process to the preceding quantities. Note that in (a) and (b) different colors stand for different tensile strains, while in (c) and (d) blue and red lines are for TM and TE polarized light, respectively.

attained at a tensile train of 2.7% for an equal doping/injection concentration of 10^{20} cm^{-3}. As in the conclusion drawn from Fig. 6, here the importance of carrier injection can also be observed. In Fig. 8 (solid, dashed and dot-dash), regardless of the strain conditions, a relative minor increase of the gain with doping level is presented when the carrier injection δn is 10^{18} cm^{-3}. On the other hand, for example, at $\epsilon = 2\%$, when keeping the doping level at 5×10^{19} cm^{-3} while changing the injection level from $\delta n = 10^{18}$ to 10^{20} cm^{-3}, the gain increases by about an order of magnitude. This observation still holds for other strain conditions. It is also interesting to point out that, though minor compared to the gain achieved by increasing the injection, higher doping usually leads to a moderate gain increase at small strain values. This increase is largely due to the reciprocal space filling in the L_c valley, which occurs under high doping concentration leading to a marginally higher carrier population in the Γ_c valley even at a small injection [43]. Finally, we note that for all of the calculated gain values, the PA process always contributes to 20%–30% of the total gain, making it an indispensable part in a credible model of optical processes in Ge.

Our calculations presented so far indicate that highly strained Ge in conjunction with high injection is the best option to attain high optical gain. However, this is probably not the case in reality when all the other injection-induced absorption processes are taken into consideration. As an example, in addition to the previously calculated gain from the recombination between CB-HH and CB-LH, we also analyzed the effect of the transition from the spin-orbit (SO) band to HH, which is believed to be a major source of extra absorption, especially at high injection [44].

Figures 9(a) and 9(b) present the gain profiles for 1.4% and 2.1% tensile strained Ge calculated from the CB-HH and CB-LH transitions (dashed lines) as well as the results after adding the SO-HH contributions (solid lines). Same quantity for relaxed Ge is also included as a comparison. It can be immediately observed that the large optical gain achieved in the previous calculation is significantly reduced by the absorption process due to the SO-HH transition. For a carrier injection level of 10^{19} cm^{-3}, the gain peak value suffers a 50% reduction for both 2.1% and 1.4% tensile strain conditions. As to an injection of 10^{20} cm^{-3}, the reduction is

even more dramatic that, as illustrated in Fig. 9(b), the optical gain is completely canceled by the strong SO-HH absorption. Indeed, at such a high carrier injection level, a large number of free holes will appear at the top of valence band, which in turn enhances the hole transitions to the SO band. This effect has already been observed by Süess and coworkers (Ref. [5], Fig. 5) in the case of a tensile strained Ge microbridge. As shown in Fig. 8, it is clear that higher injection will generally provide higher optical gain regardless of strain and doping conditions. However, the effect of SO-HH absorption process shows that there is a soft limit, typically around 5×10^{19} cm^{-3}, on the injection level that can be applied before the gain starts decreasing and eventually disappearing. On the other hand, although the SO-HH absorption can be minimized at relatively low carrier injection density, in order to achieve a usable optical gain the injection level cannot be lower than 10^{18} cm^{-3}. In fact, there are other types of absorption processes such as intraconduction band absorption (ICBA) and intravalence band absorption (IVBA) (both initial and final states are in the same band) [45] that need to be overcome. As a comment to the SO-HH absorption, we noticed that this process is predominately due to the direct transition, for the indirect absorption only accounted for about 10^{-4} of the total absorption.

We have also investigated the effect of polarization $\hat{\mathbf{e}}$ on the gain profile for a fixed tensile strain of 2.1%, which is demonstrated in Figs. 9(c) and 9(d). A similar effect of SO-HH absorption is also observed as was the case for unpolarized light. In fact, due to this absorption, the optical gain for both TM and TE modes [calculated from Eq. (A8)] is suppressed at an injection level of 10^{20} cm^{-3}. However, it should be noted that for the injection of 10^{19} cm^{-3}, the TM mode exhibited an optical gain of 4797 cm^{-1} in contrast to a much lower value of 191 cm^{-1} for TE mode as the result of transition selection rules [22].

To conclude this section on the results pertaining to Ge, we would like to point out that, although there is a general agreement on the importance of free-carrier absorption (FCA) in the Ge lasing medium, different definitions of FCA have been used in the literature [25,44,45]. In this paper, to facilitate the comparison of the absorption results from this work with others' we have treated the FCA as the combination of inter and intraconduction/valence band absorption. Consequently, the SO-HH transition is actually part of the FCA observed experimentally. As is indicated in Fig. 9, the SO-HH absorption is significant between a photon energy of 0.3–0.6 eV, but diminishes at the lower end, which corresponds to the spin-orbit split energy. We also found that, the SO-HH absorption at the photon energy corresponding to the peak optical gain calculated using our numerical model, with an injection between 10^{19} and 10^{20}cm^{-3}, reproduces the absorption cross section model presented in Ref. [44], and the corresponding hole absorption cross sections of $\sigma_h = 4.4 \times 10^{-3}$ and 9.43×10^{-3} nm^2 are obtained for relaxed and 1.4% strained Ge respectively. However, when the injection level goes above 10^{20} cm^{-3}, the SO-HH absorption increases in a logarithmic fashion with the injection level rather than linearly. This can be understood by the small density of states at SO band. At high injection (e.g., 10^{20} cm^{-3}), even the SO band starts accumulating holes, which in turn reduces the available electrons that can be excited to the HH band, leading to a reduced absorption. On the other hand, when analyzing the experimental data [44,46], the relation of FCA-hole concentration is almost linear even above $p = 10^{20}$ cm^{-3}, suggesting that other type of absorption, namely, the IVBA, is dominating. Indeed, the IVBA and ICBA can usually be modeled with the simple Drude model, which gives a linear dependence of the absorption coefficient on the carrier concentration [25]. We then conclude that the SO-HH absorption is important when the hole concentration is below 10^{20} cm^{-3}. At higher carrier concentration, the IVBA and ICBA dominate over the SO-HH transition and need to be included in the calculation instead. To our knowledge, no direct experimental data or theoretical model for IVBA and ICBA in strained Ge has been established at this time, making it difficult to estimate the overall FCA contribution. However, if one considers the experimental data of relaxed Ge available in the literature [46,47], it is clear that IVBA and ICBA will lead to a significant gain reduction for photon energies below 0.3 eV. Consequently, we speculated that the same could be true for strained Ge as well, which could make reaching lasing conditions in Ge even more challenging. As a final remark, it is worthy of note that at the highest doping and injection conditions, the Thomas-Fermi screening may not be adequate to describe the screening effect in the material. Instead, a more rigorous dynamic screening involving electron-plasma interaction should be included in the electron Green's function. As shown by Bardyszewski and coworkers [21], with this additional correction the optical gain from the CB-HH and CB-LH transitions becomes slightly larger. Nevertheless, our approach provides a baseline value for the gain and captures the most important physical phenomena which are responsible for the optical properties of strained Ge under various doping/injection conditions.

B. Silicon

In this section, we present the calculated optical properties of relaxed and strained Si using the same numerical model as we employed for Ge. Figure 10 demonstrated the absorption coefficient for unstrained intrinsic Si at different lattice temperatures. In order to compare the numerical results with the experimental data, the data of Dash and coworkers [41] measured at 77 K (open squares) and 300 K (open circles) is also plotted in Fig. 10. One can see that the results from the numerical model agree very well with the measured data. When compared to the same results obtained for Ge, we notice that for Si the PA indirect absorption process dominates the photon absorption below 3.4 eV, whereas in Ge both direct and PA indirect transition contribute to the total absorption. This makes the absorption spectrum for Si increase slowly with the photon energy in contrast to the abrupt rise observed in the Ge spectrum. The absorption spectra for different values of tensile strain have also been evaluated and presented in Fig. 11 for $\epsilon = 0\%$, 0.7%, 1.4%, and 2.1%. As is shown, when a tensile strain is applied, the absorption spectrum shifts to lower photon energy while its shape remains similar since the strain-induced shrinkage of the direct band gap has no impact on the absorption in the interested range of photon energy.

As was explained in Sec. II D, the spectral density function employed in the model describes the energy broadening of the states due to different physical phenomena, for example, phonon-electron interaction in this work. Therefore, by

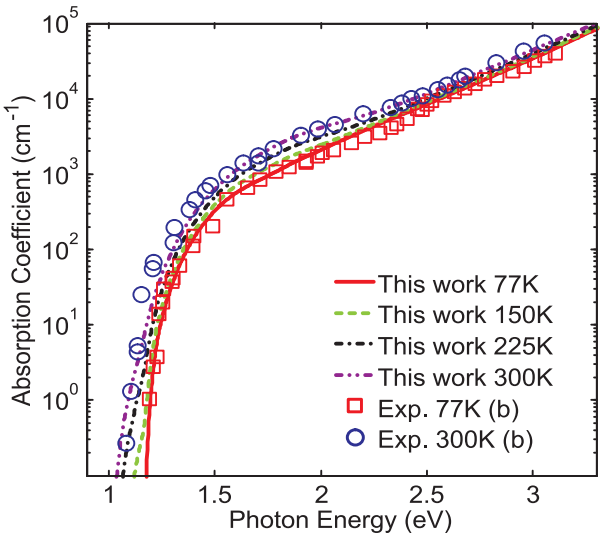

FIG. 10. (Color online) Absorption coefficient spectra for relaxed intrinsic Si at thermal equilibrium obtained from Green's function model are plotted with different lattice temperatures (colored lines). Experimental data [41] measured at the same condition are labeled by squares (77 K) and circles (300 K) as a comparison.

substituting a specific spectral density function in Eqs. (1) and (2) with a delta function, one can eliminate the PA process that pertains to a selected band transition. This enables the study of radiative processes involving multiple phonons. In particular, it is possible to study one-phonon and two-phonon assisted absorption processes in the current numerical model since two spectral functions are involved in Eqs. (1) and (2). Using this approach, we have computed the temperature dependence of the radiative recombination rate in relaxed Si, which is plotted in Fig. 12 with each curve obtained at a different lattice temperature. The Si is assumed to have an n-type doping of 10^{19} cm^{-3} and injection of 10^{18} cm^{-3}. We can notice that besides the major peak, a secondary peak to the left

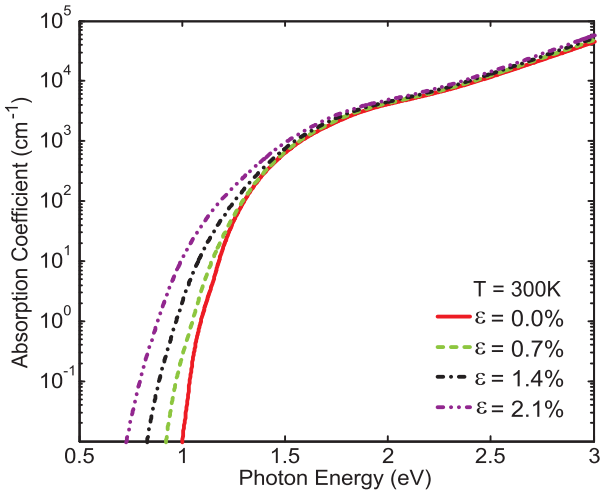

FIG. 11. (Color online) Absorption coefficient spectra for intrinsic Si at thermal equilibrium are calculated under the tensile strain of $\epsilon = 0\%$ (solid line), 0.7% (dashed line), 1.4% (dash-dot line) and 2.1% (dash-two-dot line). Lattice temperature is set at 300 K.

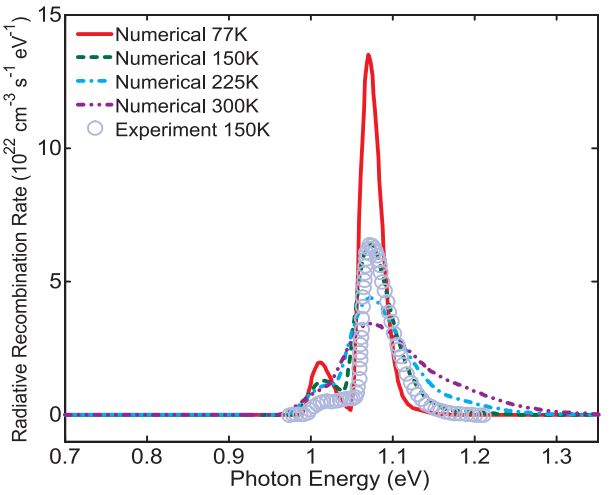

FIG. 12. (Color online) The spectra of radiative recombination rate for relaxed Si are computed with the lattice temperatures ranging from 77 to 300 K. The Si is assumed to have an n-type doping of 10^{19} cm^{-3} and injection of 10^{18} cm^{-3}. Experimental data [48] from the electroluminescence (EL) spectrum of a Si diode measured at 150 K are excerpted and converted to the same scale as the numerical result. The converted EL data (a.u.), shown in circles, has been multiplied by a constant number to fit the peak of the numerical result which is calculated at the same temperature, 150 K.

of the curves also appears at all the temperatures considered. To investigate the physical origin of the smaller peak, we have calculated the contribution of the two-phonon process and the two one-phonon processes by replacing one of the electron spectral density functions with a delta function. The results show that the two one-phonon processes separately contribute to the main peak, while the two-phonon process is responsible for the smaller peak only. In fact, the separation of the two peaks is about 60 meV, approximately equal to the energy of one optical phonon in Si, which underscores the fact that the lower peak actually represents the two-phonon event in PA process. Further validation of this result is obtained from the experimental work of Green and coworkers [48,49]. Figure 12 reports the calculated data together with the experimental data (in arbitrary units in Fig. 2(b) of Ref. [48]), which is scaled to match the maximum value of the numerical result at 150 K. While a direct quantitative comparison between our numerical data and the experimental measurements may not be possible due to the lack of information about the bias level and and the device geometry, we can see that the shape of the calculated radiative recombination curve (dashed line) and the position of the peaks are very similar to the data measured at the same temperature (150 K, open circles).

In addition to the calculated radiative recombination rates for relaxed Si, Fig. 13 presents the corresponding values when a tensile strain of $\epsilon = 1.4\%$ is applied to the system. It is noteworthy that the same low temperature carrier concentration effect, which we have mentioned in the discussion of Fig. 7, also appears in the case of relaxed Si, leading to a higher and narrower recombination peak at lower temperature. As to the results of 1.4% tensile strained Si, it is shown that the one phonon peak has broadened so much that it almost covers the two-phonon peak. This can be understood by considering

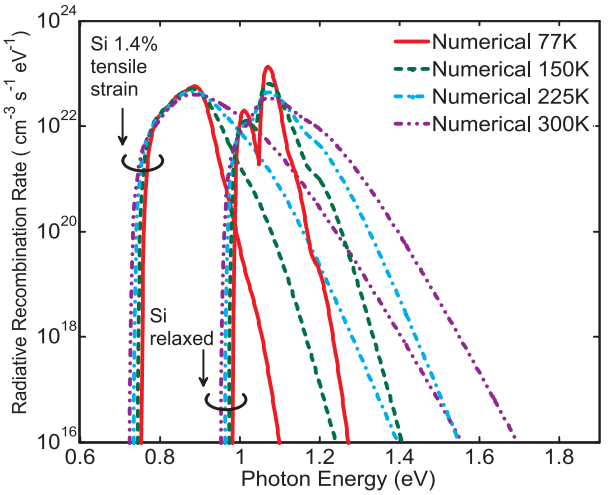

FIG. 13. (Color online) The spectra of the radiative recombination rate for relaxed (right group) and 1.4% tensile strained (left group) Si are computed with the lattice temperatures ranging from 77 to 300 K.

the change in the density of states associated to the six valleys at the conduction band minima, Δ-point. When the strain is applied, the sixfold Δ valleys split into a fourfold lower valley and a twofold upper valley, reducing the actual density of state at the conduction band edge. Consequently, in order to maintain the same carrier concentration, electrons will relocate to the higher energy states, leading to a broader radiative recombination spectrum. We want to conclude this section by comparing the spectrum for Ge presented in Fig. 7 with the one computed for Si, where it can be noticed that the two-phonon peak never appears in the plots of Ge, even in the case of relaxed material. This difference is due to several reasons. First, the conduction band density of states of relaxed Ge is similar to the one of $\epsilon = 1.4\%$ tensile strained Si. At the same doping/injection conditions, the broadening of the one-phonon peak in Ge is comparable to the strained Si, and same as the case in Fig. 13, the two-phonon peak is engulfed. Second, the small optical phonon energy in Ge makes the two-phonon peak even closer to one-phonon peak than in the case of Si. As an additional effect, this leads to the former one being even harder to distinguish from the total spectrum.

As a final note, we want to point out that based on our calculation at 300 K, with a carrier injection of 10^{18} cm^{-3} and an n-type doping of 10^{19} cm^{-3}, the optical gain at the indirect band edge of silicon is only about 10^{-2} cm^{-1}, which is orders magnitude lower than the FCA at the same photon energy [4]. In fact, Baker-Finch and coworkers [50] recently measured the FCA in 10^{19} cm^{-3} n-type doped silicon at 1110 nm and found a value of 68 cm^{-1}, which overwhelms the optical gain from phonon-assisted interband transition.

IV. CONCLUSIONS

We have developed a generalized numerical model based on the Green's function formalism and full band structures, which can be used to investigate the PA process in strained indirect band gap semiconductor materials. Deformation potential theory combined with the empirical pseudopotential model was used to generate a high-quality band structure under both relaxed and strained conditions, which ensured that all of the band anisotropy was properly described, thus eliminating the errors introduced by parabolic band approximations. We have validated the model by comparing the calculated absorption coefficient spectra of unstrained, intrinsic Ge and Si with the corresponding experimental data at 77 and 300 K. It is shown that the model can accurately reproduce the experimental data for both Ge and Si.

Using the proposed numerical model, we have calculated the radiative recombination rate of strained Ge to investigate the effect of different doping levels, injection and temperatures on the PA indirect and direct processes. These results provide additional insight into the possible ways to increase the photon emission in the material. The calculated optical gain for Ge indicates that while high carrier injection δn in tensile strained material could effectively enhance the gain through the transition of CB-HH and CB-LH, extremely high δn, regardless of the tensile strain, would inevitably suppress the total optical gain by introducing strong SO-HH absorption. Specifically, at δn in excess of 10^{20} cm^{-3}, the attainable gain from CB-HH and CB-LH is totally canceled by the SO-HH transition, leaving a net absorption in the material. We have also evaluated the gain for TE and TM polarized light. A total gain of 4749 cm^{-1} is predicted by our calculation for TM light in 2.1% tensile strained Ge with n-type doping of 10^{20} cm^{-3} and injection of 10^{19} cm^{-3}. However, by adding other types of absorption such as free carrier absorption, the achievable optical gain may be reduced.

Finally, radiative recombination properties of relaxed and strained Si were studied. We have indicated that the proposed model can indeed elucidate and reproduce the experimental data for the two-phonon events in the PA recombination process. The numerical model presented in this work is proved to be an effective tool to investigate the optical processes in indirect-gap semiconductors. In addition, this model can be further extended to inspect the nonradiative recombination mechanisms, such as Auger process, which compete with the optical gain at high-injection conditions and is currently being developed.

ACKNOWLEDGMENTS

This work was supported by the University of Pretoria, Republic of South Africa (RSA) through Grant No. 1651-5. The authors would also like to thank Professor Francesco Bertazzi (Politecnico di Torino) for his valuable comments and advices.

APPENDIX: FORMULA DERIVATION

The initial starting point of the derivation for the absorption coefficient and radiative recombination rate in Green's function theory is the total Hamiltonian for the system of interest, which includes the Hamiltonian of electrons, photons and their interaction:

$$H = \frac{1}{2m_0}[-i\hbar\nabla - e\mathbf{A}(\mathbf{r},t)]^2 + V(\mathbf{r}) + V + \sum_{\mathbf{k}} \hbar\omega_{\mathbf{k}} a_{\mathbf{k}}^{\dagger} a_{\mathbf{k}}, \quad \text{(A1)}$$

where the vector potential of the radiation field is given by

$$\mathbf{A}(\mathbf{r},t) = \frac{1}{\sqrt{N}} \sum_{\mathbf{k}} \mathbf{A}(\mathbf{k},t) e^{i\mathbf{k}\cdot\mathbf{r}},$$
$$\mathbf{A}(\mathbf{k},t) = \sqrt{\frac{\hbar}{2\omega_{\mathrm{ph}} v \epsilon}} \hat{\mathbf{e}} (a_{\mathbf{k}} e^{-i\omega_{\mathrm{ph}} t} + a^{\dagger}_{-\mathbf{k}} e^{i\omega_{\mathrm{ph}} t}). \tag{A2}$$

By neglecting the nonlinear interaction term $A^2(\mathbf{r},t)$, Eq. (A1) can be expanded and re-grouped as

$$H = H_{\mathrm{elec}} + H_{\mathrm{photon}} + H_{\mathrm{e-photon}} \tag{A3}$$

in which

$$H_{\mathrm{elec}} = -\frac{\hbar^2}{2m_0}\nabla^2 + V(\mathbf{r}) + V = \sum_{l,\mathbf{k},\sigma} E_l(\mathbf{k}) C^{\dagger}_{l,\mathbf{k},\sigma} C_{l,\mathbf{k},\sigma}, \tag{A4}$$

$$H_{\mathrm{photon}} = \sum_{\mathbf{k}} \hbar\omega_{\mathbf{k}} a^{\dagger}_{\mathbf{k}} a_{\mathbf{k}}, \tag{A5}$$

$$H_{\mathrm{e-photon}} = -\frac{e}{m_0} \mathbf{A}(\mathbf{r},t) \cdot \mathbf{P}. \tag{A6}$$

We notice that, besides the electron kinetic energy and periodic potential operators for the host crystal $V(\mathbf{r})$, H_{elec} also includes the electron-phonon and the electron-electron interaction V. As a result, the carrier energies $E(\mathbf{k})$ and the electron creation and annihilation operators $C^{\dagger}_{l,\mathbf{k},\sigma}, C_{l,\mathbf{k},\sigma}$ then represent the realistic band structure of the bulk material. In our model, this requirement is fulfilled by employing the bands from a local empirical pseudopotential model in which the screened atomic potentials are optimized to reproduce a number of experimental band data, such as: effective masses, transition energies and deformation potentials. By representing the momentum operator $\mathbf{P}$ in the base of electron eigenvectors, Eq. (A6) for a given photon frequency can be written as

$$H_{\mathrm{e-photon}} = \sum_{i,j} P_{ij} A(\mathbf{k},t) C^{\dagger}_i C_j \tag{A7}$$

with

$$P_{ij} = -\frac{e}{m_0} \langle i \,|\hat{\mathbf{e}} \cdot \mathbf{P}|\, j \rangle, \quad i,j \in \{(l,\mathbf{k},\sigma)\}, \tag{A8}$$

where i,j represent two different particle states in the band structure. Assuming that only the dipole interaction contributes to the interband transition, the number operator for electrons (holes) in band l for all the wave vectors $\mathbf{k}$ and spin states σ, is $\hat{N}_l = \sum_{\mathbf{k},\sigma} C^{\dagger}_{l,\mathbf{k},\sigma} C_{l,\mathbf{k},\sigma}$, and will commute with all the terms in Eq. (A3) except for $H_{\mathrm{e-photon}}$, which is the starting point of our derivation. In the following equations, without affecting the final results, we shall drop the time dependence of $A(\mathbf{k},t)$ and simply rewrite it as A for convenience.

Defining the system density operator as $\rho(t) = |\psi(t)\rangle\langle\psi(t)|$, the number of electrons in the conduction band can be expressed as $N_c(t) = \mathrm{Tr}[\rho(t)\hat{N}_c]$. From the Schrodinger equation, the time evolution of $\rho(t)$ can be obtained as follows:

$$\frac{\partial\rho(t)}{\partial t} = \frac{1}{i\hbar}[H,\rho(t)] \tag{A9}$$

and the time evolution of $N_c(t)$ is

$$\frac{d}{dt} N_c(t) = \frac{1}{i\hbar} \mathrm{Tr}(\rho(t)[\hat{N}_c, H]) \equiv \frac{1}{i\hbar} \langle [\hat{N}_c, H] \rangle. \tag{A10}$$

We have introduced the common notation of trace operator in Eq. (A10) and will keep using it thereafter. Applying the basic rules of commutator algebra, Eq. (A10) can be simplified as

$$[\hat{N}_c, H] = [\hat{N}_c, H_I] = \left[\sum_{\mathbf{k},\sigma} C^{\dagger}_{l_c,\mathbf{k},\sigma} C_{l,\mathbf{k},\sigma}, \sum_{i,j} P_{ij} C^{\dagger}_i C_j A \right] = \sum_{1,2} P_{1,2} C^{\dagger}_1 C_2 A \Delta^c_{1,2} \equiv H^c_I \tag{A11}$$

with

$$\Delta^c_{1,2} = \delta_{l_c,l_1} - \delta_{l_c,l_2}, \tag{A12}$$

where $\delta_{i,j}$ is the Kronecker delta function. Introducing a grand canonical ensemble, the density operator of the system at equilibrium can be written as

$$\rho_0 = e^{\frac{\Omega - \bar{H}_0}{k_B T}} \tag{A13}$$

with

$$\bar{H}_0 = H_0 - \mu_c N_c - \mu_v N_v, \tag{A14}$$

where $H_0 = H_{\mathrm{elec}} + H_{\mathrm{photon}}$ is the unperturbed system Hamiltonian and the perturbation from electron-photon interaction is $H_I = H_{\mathrm{e-photon}}$ as it will be denoted below. Ω is the thermal dynamic potential of the system and is defined through $\exp(-\Omega/(k_B T)) = \mathrm{Tr}[\exp(-\bar{H}_0/(k_B T))]$. We assume that the perturbation is adiabatically turned on at $t_0 \to -\infty$, after which the electron and hole ensembles in the conduction and valence bands remain at thermal equilibrium within themselves with the corresponding Fermi levels noted as μ_c and μ_v.

By using linear response theory, the density operator of the system can be expanded to first order as

$$\rho(t) = \rho_0 + \rho_1(t). \tag{A15}$$

Combining Eq. (A15) with Eq. (A9) and retaining the lowest order of nonvanishing terms, we have

$$i\hbar \frac{\partial\rho_1(t)}{\partial t} = [H_0, \rho_1(t)] + [H_I, \rho_0]. \tag{A16}$$

In order to find a closed form of $\rho_1(t)$ and evaluate $N_c(t)$, we consider the equivalent quantity of ρ_1 in the interaction picture $\tilde{\rho}_1(t)$, with $\rho_1(t) = e^{-iH_0 t/\hbar} \tilde{\rho}_1(t) e^{iH_0 t/\hbar}$. The time derivative of $\rho_1(t)$ is given by

$$i\hbar \frac{\partial\rho_1(t)}{\partial t} = [H_0, \rho_1(t)] + e^{-iH_0 t/\hbar} i\hbar \frac{\partial\tilde{\rho}_1(t)}{\partial t} e^{iH_0 t/\hbar}, \tag{A17}$$

and a direct comparison between Eqs. (A16) and (A17) yields

$$\tilde{\rho}_1(t) = \frac{1}{i\hbar} \int_{-\infty}^{t} [\tilde{H}_I(t'), \rho_0] dt', \tag{A18}$$

$$\tilde{H}_I(t) = e^{iH_0 t/\hbar} H_I e^{-iH_0 t/\hbar}. \tag{A19}$$

Combining Eqs. (A10), (A11), and (A18) and recalling that at equilibrium $\mathrm{Tr}(\rho_0 H_I^c) = \langle H_I^c\rangle_0 = 0$, one obtains

$$\frac{d}{dt}N_c(t) = \frac{1}{(i\hbar)^2}\int_{-\infty}^{t} dt' \langle [\tilde{H}_I^c(t), \tilde{H}_I(t')]\rangle_0, \tag{A20}$$

$$[H_I^c, H_I] = \sum_{1,2}\sum_{3,4} P_{1,2}P_{3,4}\Delta_{1,2}^c [C_1^\dagger C_2 A, C_3^\dagger C_4 A]. \tag{A21}$$

Here, $\tilde{H}_I^c(t)$ and $\tilde{H}_I(t')$ are the operators in the interaction picture of the corresponding quantities in the Schrodinger picture. To represent the commutator in Eq. (A20) in the form of Green's function, we define two new operators: $D_1 = C_1^\dagger C_2 A$ and $D_2 = C_3^\dagger C_4 A$, so that the trace of the new commutator $\langle[\tilde{D}_1(t), \tilde{D}_2(t')]\rangle_0$ can be found by first evaluating the trace below:

$$\begin{aligned}
&\langle \tilde{D}_1(t)\tilde{D}_2(t')\rangle_0 \\
&\quad = \mathrm{Tr}(\rho_0 e^{iH_0 t/\hbar} D_1 e^{-iH_0 t/\hbar} e^{iH_0 t'/\hbar} D_2 e^{-iH_0 t'/\hbar}) \\
&\quad = e^{i(t-t')(\mu_c \Delta_{1,2}^c + \mu_v \Delta 1,2^c)/\hbar} \langle d_1(t-t') d_2(0)\rangle_0,
\end{aligned} \tag{A22}$$

where the operator $d(t) = e^{i\tilde{H}_0 t/\hbar} D e^{-i\tilde{H}_0 t/\hbar}$ and Baker-Hausdorff theorem [15] has been used to simplify the noncommuting operator $\hat{N}$ and D. Equation (A20) then becomes

$$\begin{aligned}
\frac{d}{dt}N_c(t) = \frac{1}{i\hbar^2}\sum_{1,2;3,4} P_{1,2}P_{3,4}\Delta_{1,2}^c \int_{-\infty}^{t} dt' \\
\times e^{i(t-t')(\mu_c \Delta_{1,2}^c + \mu_v \Delta 1,2^c)/\hbar} G^R(1,2;3,4;t-t')
\end{aligned} \tag{A23}$$

$$G^R(1,2;3,4;t) = \frac{1}{i}\theta(t)\langle [d_1(t), d_2(0)]\rangle_0. \tag{A24}$$

As is shown, in Eq. (A24), we used the commutator instead of the anticommutator to define the three-particle retarded Green's function since the operator D consists of two fermions and one boson, making it a bosonlike operator. $\theta(t)$ is the usual unit step function. The time-dependent retarded Green's function can be further manipulated by Fourier transform and Lehmann representation [16]. Performing the procedure of frequency summation in Green's function theory, we found that $G^R(t)$ can be expressed in terms of the imaginary part of its Fourier component, which is given by

$$G^R(t) = -i\int_{-\infty}^{\infty} dE' \mathrm{Im}G^R(E') e^{iE't/\hbar}. \tag{A25}$$

Using the definition of the Dirac delta function: $\int_{-\infty}^{\infty} e^{i\omega t} dt = 2\pi\delta(\omega)$, a direct evaluation of Eqs. (A23)–(A25) yields

$$\frac{d}{dt}N_c(t) = -\frac{2\pi}{\hbar}\sum_{1,2;3,4} P_{1,2}P_{3,4}\mathrm{Im}G^R(\mu_c - \mu_v). \tag{A26}$$

We are now in the position to evaluate the retarded Green's function $\mathrm{Im}G^R(E)$, which will be derived from the Matsubara function of the system. Define the three-particle Matsubara function $g(\tau)$ as

$$g(\tau) = -\langle T_\tau (C_1^\dagger(\tau) C_2(\tau) A(\tau) C_3^\dagger(0) C_4(0) A(0))\rangle \tag{A27}$$

with

$$C_i(\tau) = e^{\tilde{H}\tau/\hbar} C_i e^{-\tilde{H}\tau/\hbar}, \quad \tau \equiv it, \tag{A28}$$

where T_τ is the τ-ordering operator which arranges the operators with the earliest τ to the rightmost. Though Eq. (A27) can be calculated to any order by expanding the corresponding Dyson's equation, we shall only retain the lowest order of $g(\tau)$ by using the free-particle Green's function of photons to approximate each term obtained by applying Wick's theorem to Eq. (A27) [15]. As a result, this approximation will ignore the polariton effect in the solid and consequently assuming that only electrons will interact with phonons. It should be noted that we did not approximate the electron Green's function with its free-particle one. Instead, we formally adopt the full Green's function of electrons (holes) and put the discussion about its specific form in Sec. II B, where the electron self-energy including the related four kinds of electron-phonon interaction is presented. From Wick's theorem,

$$g(\tau) \simeq -\langle T_\tau (C_1^\dagger(\tau) C_2(\tau) C_3^\dagger(0) C_4(0))\rangle \langle T_\tau A(\tau) A(0)\rangle . \tag{A29}$$

The photon part is given by [15]

$$g_{\mathrm{ph}}(\tau) \equiv \langle T_\tau A(\tau) A(0)\rangle \simeq \frac{\hbar}{2\omega_{\mathrm{ph}} \upsilon\epsilon} e^{-\tau\omega_{\mathrm{ph}}}\theta(\tau), \tag{A30}$$

and the electron part can be formally written as

$$\begin{aligned}
g_2(\tau) =& -\langle T_\tau C_1^\dagger(\tau) C_2(\tau)\rangle \langle T_\tau C_3^\dagger(0) C_4\rangle \\
&+ \langle T_\tau C_4(0) C_1^\dagger(\tau)\rangle \langle T_\tau C_2(\tau) C_3^\dagger(0)\rangle \\
=& -\delta_{1,2}\delta_{3,4} n_1 n_3 + g_{2,3}(\tau) g_{4,1}(-\tau)\delta_{2,3}\delta_{4,1}
\end{aligned} \tag{A31}$$

with

$$g_{2,3}(\tau) = \langle T_\tau C_2(\tau) C_3^\dagger(0)\rangle, \quad \tau > 0, \tag{A32}$$

$$g_{4,1}(\tau) = \langle T_\tau C_4(\tau) C_1^\dagger(0)\rangle, \quad \tau < 0. \tag{A33}$$

Here, Eqs. (A32) and (A33) are the full Matsubara functions for one fermion (electron, hole). The same technique used in deriving Eq. (A25) can also be used to represent Eqs. (A32) and (A33) in terms of the imaginary parts of the corresponding electron retarded Green's function. With $\tau > 0$, we find that

$$g_{2,3}(\tau) = \frac{1}{\pi}\int_{-\infty}^{\infty} dE_1' \mathrm{Im}G_{2,3}^R(E_1') e^{-\tau E_1'/\hbar}\Theta(E_1'), \tag{A34}$$

$$g_{4,1}(-\tau) = \frac{1}{\pi}\int_{-\infty}^{\infty} dE_2' \mathrm{Im}G_{4,1}^R(E_2') e^{\tau E_2'/\hbar}[1-\Theta(E_2')]. \tag{A35}$$

Combining Eqs. (A29), (A30), (A34), and (A35), and substituting $i\omega_n$ with $\omega + i\delta$ to get the retarded Green's function from the Matsubara function, the system retarded Green's function in Eq. (A26) becomes

$$\begin{aligned}
\mathrm{Im}G^R(E) =& \frac{\hbar}{4\pi^2\omega_{\mathrm{ph}}\upsilon\epsilon}\int_{-\infty}^{\infty} dE_1' \int_{-\infty}^{\infty} dE_2' \\
&\times \Theta(E_1')[1-\Theta(E_2')]\mathrm{Im}G_{2,3}^R(E_1')\mathrm{Im}G_{4,1}^R(E_2') \\
&\times \delta(E + E_2' - E_1' - \hbar\omega_{\mathrm{ph}})\delta_{2,3}\delta_{4,1}.
\end{aligned} \tag{A36}$$

One should be aware that in the derivation above, we have always assumed that the time in the Green's function fulfills the condition $t > 0$. In the case of $t < 0$, however, the physical process reverses, i.e., the transition from band 1 to band 2 reverses as well. Consequently, when considering the total absorption for the material, both processes need to be involved and a reverse term should be added to Eq. (A36). This will lead to a similar equation as Eq. (A36) except that the Fermi factor now becomes $\Theta(E_1') - \Theta(E_2')$ to account for the net absorption from band 1 to band 2. In the case of the radiative recombination rate, only one process should be included and Eq. (A36) gives the correct Green's function. Using these relations,

$$\alpha(\hbar\omega_{\rm ph}) = \frac{dN_c}{dt} \Big/ \left(\frac{I}{\hbar\omega_{\rm ph}}\right), \tag{A37}$$

with $I = \hbar\omega_{\rm ph} n c_0/4v$ and remembering that the subscript 1, 2, ... represent a group of states in the band structure $(l,\mathbf{k},\sigma)$, the final expression for the net absorption coefficient between band 1 and 2 (assuming that $E_2(\mathbf{k}) > E_1(\mathbf{k})$) is

$$\begin{aligned}\alpha_{12}(\hbar\omega_{\rm ph}) = {} & \frac{2\pi}{n_r c_0 v \omega_{\rm ph}\epsilon_0} \sum_{\mathbf{k}} |P_{1,2}(\mathbf{k})|^2 \\ & \times \int dE_1' \int dE_2' (\Theta(E_1') - \Theta(E_2')) \\ & \times \delta(\mu_c - \mu_v + E_2' - E_1' - \hbar\omega_{\rm ph}) \\ & \times {\rm Im}G_{l_1}^R(\mathbf{k}, E_1') {\rm Im}G_{l_2}^R(\mathbf{k}, E_2'). \end{aligned} \tag{A38}$$

The corresponding radiative recombination rate per unit volume per energy interval from band 2 to band 1, therefore becomes

$$\begin{aligned}R_{21}(\hbar\omega_{\rm ph}) = {} & \frac{2n_r\omega_{\rm ph}}{\pi\hbar c_0^3 v \epsilon_0} \sum_{\mathbf{k}} |P_{1,2}(\mathbf{k})|^2 \\ & \times \int dE_1' \int dE_2' \Theta(E_2')(1 - \Theta(E_1')) \\ & \times \delta(\mu_c - \mu_v + E_2' - E_1' - \hbar\omega_{\rm ph}) \\ & \times {\rm Im}G_{l_1}^R(\mathbf{k}, E_1') {\rm Im}G_{l_2}^R(\mathbf{k}, E_2'). \end{aligned} \tag{A39}$$

[1] P. Boucaud, M. El Kurdi, A. Ghrib, M. Prost, M. de Kersauson, S. Sauvage, F. Aniel, X. Checoury, G. Beaudoin, L. Largeau, I. Sagnes, G. Ndong, M. Chaigneau, and R. Ossikovski, Photon. Res. **1**, 102 (2013).

[2] M. Virgilio, C. L. Manganelli, G. Grosso, G. Pizzi, and G. Capellini, Phys. Rev. B **87**, 235313 (2013).

[3] R. Soref, J. Hendrickson, and J. W. Cleary, Opt. Express **20**, 3814 (2012).

[4] D. Liang and J. Bowers, Nat. Photon. **4**, 511 (2010).

[5] M. J. Süess, R. Geiger, R. A. Minamisawa, G. Schiefler, J. Frigerio, D. Chrastina, G. Isella, R. Spolenak, J. Faist, and H. Sigg, Nat. Photon. **7**, 466 (2013).

[6] J. Liu, X. Sun, R. Camacho-Aguilera, L. C. Kimerling, and J. Michel, Opt. Lett. **35**, 679 (2010).

[7] G. Capellini, G. Kozlowski, Y. Yamamoto, M. Lisker, C. Wenger, G. Niu, P. Zaumseil, B. Tillack, A. Ghrib, M. de Kersauson, M. El Kurdi, P. Boucaud, and T. Schroeder, J. Appl. Phys. **113**, 013513 (2013).

[8] O. Aldaghri, Z. Ikoni, and R. W. Kelsall, J. Appl. Phys. **111**, 053106 (2012).

[9] M. El Kurdi, H. Bertin, E. Martincic, M. De Kersauson, G. Fishman, S. Sauvage, A. Bosseboeuf, and P. Boucaud, Appl. Phys. Lett. **96**, 041909 (2010).

[10] C. Boztug, J. R. SnchezPrez, F. F. Sudradjat, R. B. Jacobson, D. M. Paskiewicz, M. G. Lagally, and R. Paiella, Small **9**, 622 (2013).

[11] M. du Plessis, P. J. Venter, and E. Bellotti, IEEE J. Quantum Electron. **49**, 570 (2013).

[12] P. J. Venter, M. du Plessis, A. W. Bogalecki, and C. J. van Rensburg, *Optoelectronic Integrated Circuits XV*, Proceedings SPIE Vol. 8628 (SPIE, Bellingham, WA, USA, 2013), p. 86280A.

[13] P. J. Venter, A. C. Alberts, M. du Plessis, T. H. Joubert, M. E. Goosen, C. J. van Rensburg, P. Rademeyer, and N. M. Faure, *Advances in Display Technologies III*, Proceedings SPIE Vol. 8643 (SPIE, Bellingham, WA, USA, 2013), p. 864309.

[14] J. Bude, N. Sano, and A. Yoshii, Phys. Rev. B **45**, 5848 (1992).

[15] G. D. Mahan, *Many-Particle Physics*, 2nd ed. (Plenum Press, New York, USA, 1993).

[16] M. Takeshima, Phys. Rev. B **26**, 917 (1982).

[17] M. Takeshima, J. Appl. Phys. **56**, 49 (1984).

[18] F. Bertazzi, M. Goano, and E. Bellotti, Appl. Phys. Lett. **101**, 011111 (2012).

[19] M. Takeshima, Phys. Rev. B **25**, 5390 (1982).

[20] N. H. Kwong, G. Rupper, and R. Binder, Phys. Rev. B **79**, 155205 (2009).

[21] W. Bardyszewski and D. Yevick, Phys. Rev. B **39**, 10839 (1989).

[22] S. Chuang, *Physics of Photonic Devices* (John Wiley & Sons, Inc., Hoboken, New Jersey, 2009).

[23] W. Bardyszewski and D. Yevick, J. Appl. Phys. **58**, 2713 (1985).

[24] B. K. Ridley, *Quantum Processes in Semiconductors* (Oxford University Press Inc., New York, 1999).

[25] S. Adachi, *Properties of Group-IV, III-V and II-VI Semiconductors* (John Wiley & Sons Ltd., Chichester, 2005).

[26] M. V. Fischetti and S. E. Laux, J. Appl. Phys. **80**, 2234 (1996).

[27] *Semiconductors: Data Handbook*, edited by O. Madelung, 3rd ed. (Springer-Verlag, Berlin, Heidelberg, Germany, 2004).

[28] B. D. Malone and M. L. Cohen, J. Phys.: Condens. Matter **25**, 105503 (2013).

[29] M. Goano, E. Bellotti, E. Ghillino, G. Ghione, and K. F. Brennan, J. Appl. Phys. **88**, 6467 (2000).

[30] J. Kim and M. Fischetti, J. Appl. Phys. **108**, 013710 (2010).

[31] F. Bertazzi, M. Moresco, and E. Bellotti, J. Appl. Phys. **106**, 063718 (2009).

[32] G. Weisz, Phys. Rev. **149**, 504 (1966).

[33] S. Bloom and T. K. Bergstresser, Solid State Commun. **6**, 465 (1968).

[34] J. P. Walter, M. L. Cohen, Y. Petroff, and M. Balkanski, Phys. Rev. B **1**, 2661 (1970).

[35] F. Herman, C. D. Kuglin, K. F. Cuff, and R. L. Kortum, Phys. Rev. Lett. **11**, 541 (1963).
[36] E. Clementi and C. Roetti, At. Data Nucl. Data Tables **14**, 177 (1974).
[37] D. R. Mašović and F. R. Vukajlović, Comp. Phys. Comm. **30**, 207 (1983).
[38] G. Lehmann and M. Taut, Phys. Stat. Sol. (B) **54**, 469 (1972).
[39] C. Jungemann and B. Meinerzhagen, *Hierarchical Device Simulation The Monte-Carlo Perspective* (Springer Verlag, Wien, New York, USA, 2003).
[40] A. H. MacDonald, S. H. Vosko, and P. T. Coleridge, J. Phys. C **12**, 2991 (1979).
[41] W. C. Dash and R. Newman, Phys. Rev. **99**, 1151 (1955).
[42] H. Wen and E. Bellotti, J. Electron. Mater. **43**, 2841 (2014).
[43] B. Dutt, D. S. Sukhdeo, D. Nam, B. M. Vulovic, Z. Yuan, and K. C. Saraswat, IEEE Photon. J. **4**, 2002 (2012).
[44] L. Carroll, P. Friedli, S. Neuenschwander, H. Sigg, S. Cecchi, F. Isa, D. Chrastina, G. Isella, Y. Fedoryshyn, and J. Faist, Phys. Rev. Lett. **109**, 057402 (2012).
[45] J. Liu, X. Sun, D. Pan, X. Wang, L. C. Kimerling, T. L. Koch, and J. Michel, Opt. Express **15**, 11272 (2007).
[46] R. Newman and W. W. Tyler, Phys. Rev. **105**, 885 (1957).
[47] W. G. Spitzer, F. A. Trumbore, and R. A. Logan, J. Appl. Phys. **32**, 1822 (1961).
[48] M. A. Green, J. Zhao, A. Wang, P. J. Reece, and M. Gal, Nature (London) **412**, 805 (2001).
[49] T. Trupke, M. A. Green, P. Wurfel, P. P. Altermatt, A. Wang, J. Zhao, and R. Corkish, J. Appl. Phys. **94**, 4930 (2003).
[50] S. Baker-Finch, K. McIntosh, D. Yan, K. Fong, and T. Kho, J. Appl. Phys. **116**, 063106 (2014).